Bachelor's Thesis

Active Magnetic Field Stabilisation for a Quantum Gas Microscope

Ranga Rosok

August 16, 2021

Examiner: Prof. Dr. Tilman Pfau

Advisor: Dr. Sean Graham

Submitted to

University of Stuttgart
5th Institute of Physics
Pfaffenwaldring 57, 70569 Stuttgart

Abstract

In our upcoming dysprosium quantum gas microscope experiment we require a magnetic field stability on the level of about 5 nT. Field stability at this level will allow us to address a 1000 nm narrow transition in dysprosium necessary for achieving single-site resolution in an 180 nm lattice. The challenge is to reduce the fluctuations of the magnetic field in the experiment, so that the linewidth of this narrow transition can be resonantly probed. One proposed method for the stabilisation is to use a μ-metal shield, but this produces a gradient of the magnetic field at the position of the atoms if coils are used offset to the centre to the shield. In addition, the shield will also distort magnetic fields being used outside of the shield. The goal of this thesis is to develop and test an alternative method, the active magnetic field stabilisation. The used system consists of three equal square Helmholtz coils, which are controlled by a digital PID controller to cancel out magnetic field noise. The result of the stabilisation in all three directions was a root mean square norm magnetic field noise of $|\mathbf{B}_{\text{RMS}}| = 11\,\text{nT}$. The field was stabilised at frequencies from DC to 150 Hz. This result shows that an active magnetic field stabilisation may be a viable solution for the stabilisation of the transition energy, if further improvements are made.

Kurzzusammenfassung

In unserem geplanten Dysprosium Quantengas Mikroskop Experperiment brauchen wir eine Stabilität des Magentfeldes von 5 nm. Diese Stabilität ermöglicht es uns, einen schmalbandingen Übergang in Dysprosium anzuregen, welcher notwendig ist, um eine Auflösung von 180 nT zu ereichen. Die Herausforderung dabei ist es, das Magnetfeld in dem Experiment so konstant zu halten, dass die Übergangsfrequenz stabil ist. Eine vorgeschlagene Methode ist der Gebrauch eines μ-Metal Käfigs, welcher allerdings zu einem Gradientenfeld bei nicht symmetrischer Spulenanordnung innerhalb des Käfigs führt und ausserhalb andere erzeugte Magnetfelder deformiert. Das Ziel dieser Arbeit ist es, eine alternative Lösung zu ermitteln und zu testen - die aktive Magnefeldstabilisierung. Der benutzte Aufbau umfasst drei baugleiche Helmholtz-Spulenpaare, die von einem digitalen PID angesteuert werden, um das Magnetfeld zu stabilisieren. Dieses System erreichte eine Stabilisierung in alle drei Raumrichtungen von einem quadratischen Mittelwert des Magnetischefeldrauschens von $|\mathbf{B}_{\text{RMS}}| = 11\,\text{nT}$. Die Stabilisierung wurde in einem Frequenzbereich von $0 - 150\,\text{Hz}$ erzielt. Dieses Ergebnis zeigt, dass dieser Ansatz eine mögliche Lösung zur Stabilisierung der Übergangsfrequenz ist, wenn weitere Verbesserungen vorgenommen werden.

Ehernwörtliche Erkärung

Gemäß der Prüfungsordnung der Universität Stuttgart für den Bachelorstudiengang Physik vom 31. Juli 2015 versichere ich,

1. dass ich diese Arbeit selbst verfasst habe,
2. dass ich keine anderen als die angegebenen Quellen benutzt und alle wörtlich oder sinngemäß aus anderen Werken übernommenen Aussagen als solche gekennzeichnet habe
3. dass die eingereichte Arbeit weder vollständig noch in wesentlichen Teilen Gegenstand eines anderen Prüfungsverfahrens gewesen ist und
4. das elektronische Exemplar mit den anderen Exemplaren übereinstimmt.

Stuttgart, 16.08.2021
Ort, Datum

Unterzeichner

Contents

1 Introduction

In the 5th Institute of Physics of the University of Stuttgart the dysprosium team is exploring new states of matter and collective behavior of ultra cold dipolar quantum gases. Recent results in our group show density changes of these dipolar quantum gases across the superfluid-supersolid phase transition [1] or roton excitations in a dipolar quantum gas [2]. All the data collected in these experiments is done on an machine that was built in 2000. Its first intend use case was for Chromium atoms and not for the now used Dysprosium atoms. Dysprosium is an element with one of the highest magnetic moments of 10 μ_B [3]. This large magnetic moment makes the gas dipolar and enables long range-interaction, where not only next-neighbour interaction are taken int account. The experiment was modified in the year 2011 to fit the requirements for experiments with Dysprosium, after Benjamin Lev and his group discovered a Bose-Einstein condensate of Dysprosium [4]. In 2017 the planning of a new generation of the experiment was started. This should make the use of the gained knowledge with the current setup and transfer it to the next design to improve the observations and results. An example that can be named is to discovers for example new states of matter [5]. A way to achieve this, is to plan the experiment in such a high precision that even the smallest screw or spring is made out of materials that do not interfere with the magnetic field. A render of the current state of the planning is displayed in Fig. 1.

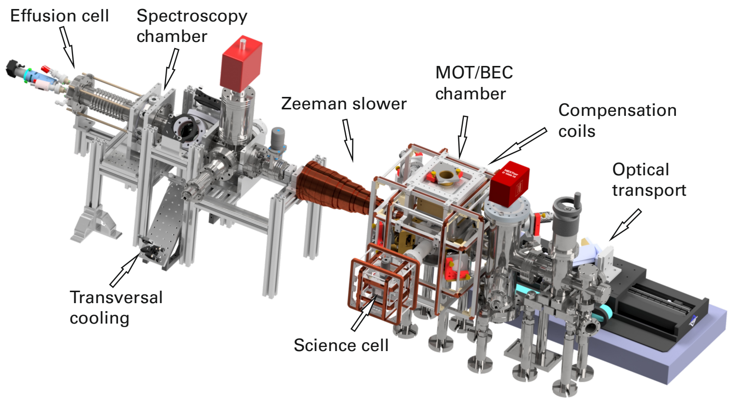

Figure 1: Rendered image of the next generation of the Dysprosium Experiment at the 5th Institute of Physics of the University of Stuttgart (As at August 2021).

A second improvement that will come with this setup is the quantum gas microscope. This will make it possible to perform quantum simulations like Richard Feynman has proposed [6]. A possible goal is to understand high temperature super-conductivity by making use of the extended Bose- and Fermi-Hubbard model.
This microscope is partly displayed in Fig. 1, it will sit on science cell next to the right side of the MOT chamber. It will resolve single atoms of Dysprosium with an resolution of 180 nm. The atoms sit in the science chamber to close to each other, that they cant

be resolved at the same time. To solve this issue most of the atoms are exited to a long lived state (called an inner-shell state in Fig. 2). The corresponding small line width of $\sim 10\,\mathrm{Hz}$ leads to the fact that these states are challenging to image with a fluctuating magnetic field. After one picture is taken atoms in the excited state are emptied and most of the atoms are in the initial ground state again. This process can be done multiple times. A challenge is to keep the energy distance between the two states constant, so the laser frequency can reaches this narrow line width from the ground state. Due the high sensitivity of the Dysprosium atoms to the magnetic field the Zeeman shift will also be large, so the field has to be kept stable to ensure that the laser is resonant with the transition frequency.

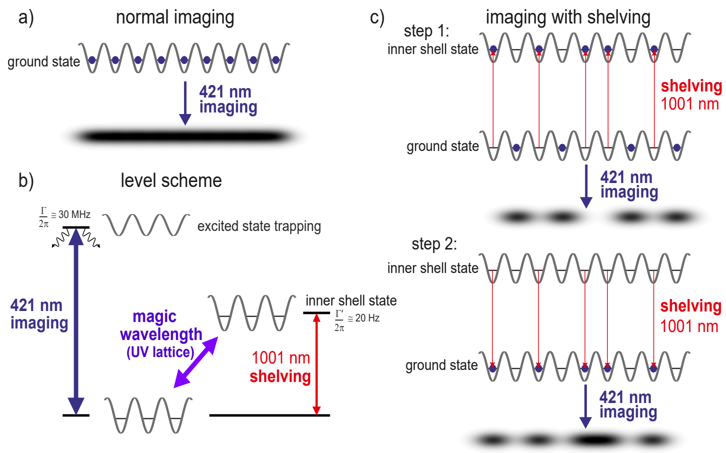

Figure 2: Concept of super-resolution imaging technique. Before taking a picture a part of the atoms will be exited with an inner-shell transition (b)), where they can not be addressed by the imaging laser . After taking the first part of the picture the atoms are relaxed and the same procedure can be repeated (c)) step 2).

The initial design to compensate the fluctuations is to use a shield out of the a metal with huge magnetic permeability. This can passively compensate the fluctuations of the magnetic field. The other flaw of the available μ-metal ($\mu_r \approx 10.000$) shield is that the science chamber where the atoms are addressed by the laser light is not in the middle of the cage (see Fig. 8). An applied magnetic field inside the shield would mirror coils from the highly magnetic μ-metal walls. Due to the offset of the science chamber from the center, the magnetic field will be distorted from this reflection and has a gradient that leads to spatially different transition wavelength.

An alternative solution is an active magnetic field stabilization. In a complete replacement of the shield this method will not only eliminate the reflection issue, it also gives control of the magnetic field and makes it easier to access the science chamber with for example the laser light.

This thesis will provide the planing, building and testing for an possible active magnetic field stabilisation approach.

2 Coil Design

In the 19th century James Clerk Maxwell, continued the work of previous physicists, like Coulomb and Ampere and published his well known equations, the so called Maxwell equations, Eqn. (2.1) - Eqn. (2.4)[7]. The Maxwell equations are the foundation of every electrical and magnetic phenomena. They consist of four coupled differential equations. In a material they look in SI units as followed

$$\nabla \cdot \mathbf{D} = \rho \tag{2.1}$$

$$\nabla \cdot \mathbf{B} = 0 \tag{2.2}$$

$$\nabla \times \mathbf{E} = -\frac{\partial \mathbf{B}}{\partial t} \tag{2.3}$$

$$\nabla \times \mathbf{H} = \mathbf{j} + \frac{\partial \mathbf{D}}{\partial t}. \tag{2.4}$$

The free charge density is by ρ denoted and the current density by $\mathbf{j}$. The magnetic flux density $\mathbf{B}$ changes inside of matter to the so called magnetic field $\mathbf{H}$. Same is valid for the electric field $\mathbf{E}$ without matter and the electric displacement field $\mathbf{D}$ with matter. They both are connected through the magnetization vector $\mathbf{M}$ or the polarization density $\mathbf{P}$

$$\mathbf{D} = \epsilon_0 \, \mathbf{E} + \mathbf{P} = \epsilon_0 \epsilon_r \, \mathbf{E} \tag{2.5}$$

$$\mathbf{B} = \mu_0 (\mathbf{H} + \mathbf{M}) = \mu_0 \mu_r \mathbf{H}. \tag{2.6}$$

For the most materials with small fields $\mathbf{P}$ and $\mathbf{M}$ are linear dependent of the electric field $\mathbf{E}$ or the magnetic flux density $\mathbf{B}$. In Eqn. (2.6) this is taken into account by the introduction of the two parameters ϵ_r and μ_r, which are the relative permittivity and permeability. For vacuum, through definition, $\mu_r = 1$ and approximately also for air. The magnetic permeability μ_r is for the most diamagnetic and paramagnetic materials also close to 1, which will become later important for experiment. If there is a interface between to materials with different μ_r the magnetic field will be distorted, because

$$\mathbf{n} \cdot (\mathbf{B}_1 - \mathbf{B}_2) = 0 \tag{2.7}$$

$$\mathbf{n} \times \left(\frac{\mathbf{B}_1}{\mu_1} - \frac{\mathbf{B}_2}{\mu_2}\right) = \mathbf{i}. \tag{2.8}$$

For a dielectric and for static magnetic fields the surcface current density vanishes and the two $\mathbf{B}$ field have different normal components. Only if μ_r is similar this distortion could be neglected. Most of the time the predominant material is air with $\mu_r \approx 1$, what means that all other materials should have similar values. To name a few examples

- copper $\mu_r = 1 - 0.98\,10^{-5}$
- aluminium $\mu_r = 1 + 2.3\,10^{-5}$
- PEEK $\mu_r = 1 - 0.93\,10^{-5}$
- PLA $\mu_r \approx 1 - 0.5\,10^{-5}$ [8, 9].

This theory will be important if the goal of an experiment is to produce a homogeneous magnetic field. The later on used materials are mainly the listed ones. This also helps with the naming. The four possible option can be reduced to two, where the relationship

$$\mathbf{D} \approx \epsilon_0 \, \mathbf{E} \tag{2.9}$$

$$\mathbf{B} \approx \mu_0 \, \mathbf{H} \tag{2.10}$$

is valid. Due to this fact and for easier reading, it is only talked about **E** and **B** in the following text, if not otherwise noted.

2.1 Theory of Electromagnetism and Helmholtz Coils

For the calculations of magnetic fields, produced by coils, many simplifications of the Maxwell equations, Eqns. (2.1) to (2.4), can be done. The linearization of **D** and **H** was already mentioned in Eqn. (2.10). For static magnetic fields the charge density ρ is constant, which means

$$\frac{\partial \rho}{\partial t} = 0. \tag{2.11}$$

This directly leads to the fact that the electric field **E** is also not time dependent and due to the static magnetic field it has rotation. The only interesting remaining Maxwell equation is Eqn. (2.4) and will transform into

$$\nabla \times \mathbf{B} = \mu_0 \, \mathbf{j}. \tag{2.12}$$

Combining with Eqn. (2.2), a vector potential **A** can be formed to describe the magnetic field completely

$$\mathbf{B} = \nabla \times \mathbf{A}. \tag{2.13}$$

To figure out the explicit form of this vector potential it is helpful to make use of the result taken back in the year 1820 by Biot and Savart, the so called Biot-Savart law [7]. It connects the differential of the magnetic field **B** directly with current I, that runs through an infinitesimal line element $d\mathbf{l}$

$$d\mathbf{B} = \frac{\mu_0}{4\pi} \, I \, \frac{d\mathbf{l} \times \mathbf{x}}{|\mathbf{x}|^3}. \tag{2.14}$$

The current I times the small line element $d\mathbf{l}$ is simmilar to the current density $\mathbf{j}(\mathbf{x})$ times the infinitesemal volume dV. With this the Biot-Savart law can be rewritten and integrated over all three dimensions, that results in

$$B = \frac{\mu_0}{4\pi} \int \mathbf{j}(\mathbf{x}') \times \frac{\mathbf{x} - \mathbf{x}'}{|\mathbf{x} - \mathbf{x}'|^3} \, d^3x'. \tag{2.15}$$

In most cases it is not recommended to calculate this integral directly. At this point the vector potential is used. It its possible to rewrite the integral to

$$B = \frac{\mu_0}{4\pi} \, \nabla \times \int \frac{\mathbf{j}(\mathbf{x}')}{|\mathbf{x} - \mathbf{x}'|} \, d^3x', \tag{2.16}$$

with the knowledge that the fraction in Eqn. (2.15) is just a derivative of the corresponding term in Eqn. (2.16). This equation is now a lot easier to solve and very similar to the equations which are known from the electrostatic theory. It is also now easy to recognize the vector potential $\mathbf{A}$ from Eqn. (2.13).

2.1.1 Generating a Magnetic Field

The calculation in Section 2.1 with the result of Eqn. (2.16) is the proof that it is possible to create and control magnetic fields with only a current density $\mathbf{j}(\mathbf{x})$. The next important step is to find a suitable current density configuration that creates the demanded field. The easiest way to control $\mathbf{j}$, is to make use of wires in which a charge flows in a defined direction. If the order of the geometric path is way bigger than the diameter of the wire this current density can be reduced to a one dimensional line. This is in most of the cases valid for any wire configuration under normal conditions. With this knowledge the magnetic field of a simple loop can be calculated. In Fig. 3 the layout and the labeling are shown.

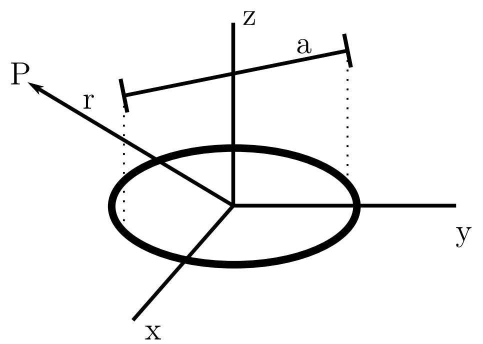

Figure 3: Centered conducting loop with a diameter a, represented by the bold circle. P is the point at which the magnetic field is calculated an r the corresponding vector.

In this configuration the current density is described by

$$J_\varphi = I\ \sin\vartheta' \delta(\cos\vartheta') \frac{\delta(r' - (a/2))}{a/2}, \tag{2.17}$$

which is a one dimensional loop. The vector potential $\mathbf{A}$, which is in this case only A_φ, can be calculated with Eqn. (2.16). It has for this highly symmetrical configuration for every point in space an more or less easy solution [7]. It is given by

$$A_\varphi(r,\varphi) = \frac{\mu_0}{4\pi} \frac{4\,I(a/2)}{\sqrt{(a/2)^2 + r^2 + 2\,(a/2) r \sin\vartheta}} \left[\frac{(2-k^2)K(k) - 2\,E(k)}{k^2}\right]. \tag{2.18}$$

The functions $E(k)$ and $K(k)$ are the complete elliptical integrals first and second kind with the parameter

$$k^2 = \frac{4\,(a/2)\,r\,\sin\vartheta}{(a/2)^2 + r^2 + 2\,(a/2)\,r\,\sin\vartheta}. \tag{2.19}$$

The exact expression of the field is for the following not important, but the general shape of the solution is of great interest and shown in Fig. 4. The magentic field shape is further discussed in Section 2.1.2. It is shown in .

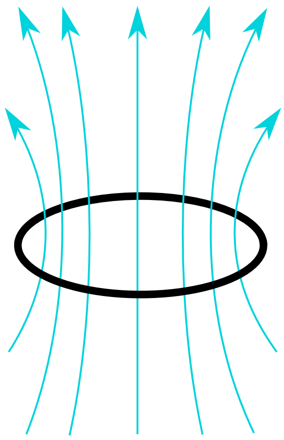

Figure 4: Magnetic field generated be a single conducting loop. The magnetic field lines point through the loop following the right-hand rule for the current I flowing in the loop.

2.1.2 Magnetic Field of Different Coil Shapes

Fig. 4 shows the $\mathbf{B}$ field of a single circular coil. Due to that fact that the electromagnetism is a linear theory one can sum up multiple parts of the field which contribute to a total field. This is not a new fact, it is already visible in Eqn. (2.15). So if one would add another loop in a clever way one can achieve a magnetic field pattern, which is very uniform at a specific point. A possible, good, configuration are the so called Helmholtz coils. These consist, as foreshadowed, of two circular coils, which have a specific distance d between the two coils. This distance is important, because as one can easily imagine with the $\mathbf{B}$ pattern of a single loop, by adding them up with a varying distance d there is a value at which $\mathbf{B}$ has not only a local extremum in the center point, but also the second derivative in the direction of z vanishes. This means

$$\frac{\partial^2}{\partial z^2}\mathbf{B}(\rho = 0, z) = 0. \tag{2.20}$$

The magnetic field at $\rho = 0$ gets a simple expression [8] which looks as follows

$$\mathbf{B}(\rho = 0, \mathbf{z}) = \left(\frac{\mu_0\, I_1\, n_1\, (a_1/2)^2}{2((a_1/2)^2 + (z - d/2)^2)^{3/2}} + \frac{\mu_0\, I_2\, n_2\, (a_2/2)^2}{2((a_2/2)^2 + (z + d/2)^2)^{3/2}} \right) \hat{\mathbf{e}}_z. \tag{2.21}$$

This expression can be derived with Eqn. (2.18), if two coils are used which have a distance of d. The n is in this case the number of turns, which can be just multiplied, because it is a linear theory. By design, both of the coils are the same $a_1 = a_2,\ n_1 = n_2$ and have the same amount of current running through $I_1 = I_2$. This leads then to the important result of

$$a = 0.5\, d \tag{2.22}$$

which is the optimal distance between two coils for a homogeneous field. This distance d also determines the name "Helmholtz configuration." The second option is to use a set of two square coils. They are a bit easier to manufacture, if they are not wound on a cylinder. In this case it is possible to use metal profiles to make a framework for the coils. The final and the determining factor for the decision to not use these round coils and instead go with square ones is that the square type has a approximately the same area where the field is uniform, keeping the same dimensions at both coil types[10].
Because of the different geometry of the square coils, the magnetic field and the distance d to achieve Helmholtz configuration is also slightly different. To determine the right d many studies were conducted [11, 12] with the result that the distance changes to

$$d = 0.5445\, a. \tag{2.23}$$

This is only a small increase compared to the circular coils design, Eqn. (2.22). To calculate the magnetic field it is again a good method to make use of the vector potential $\mathbf{A}$ to get finally $\mathbf{B}$, compare to Eqn. (2.13). The general idea behind the overall potential is to add up the potential of a single straight conducting wire. Each of these single conducting wires represent one side of the loop times the number of windings n. The total potential is given by [13]

$$A_x(\mathbf{r}) = \frac{\mu_0\, n\, I}{4\pi} \ln\left[\frac{r_1 + (a/2) + x}{r_2 - (a/2) + x} \cdot \frac{r_3 - (a/2) + x}{r_4 + (a/2) + x}\right], \tag{2.24}$$

and

$$A_y(\mathbf{r}) = \frac{\mu_0\, n\, I}{4\pi} \ln\left[\frac{r_2 + (b/2) + y}{r_3 - (b/2) + y} \cdot \frac{r_4 - (b/2) + y}{r_1 + (b/2) + y}\right], \tag{2.25}$$

where the I is the current and the other constants represent the geometrical layout of the coil shown in Fig. 5. The variable r_i represents the distance from the corresponding corner to the point at $\mathbf{r}$.

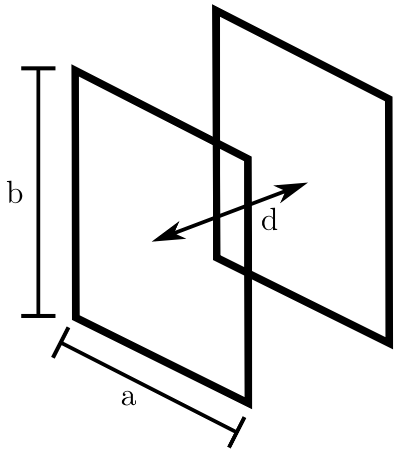

Figure 5: Pair of two square coils with the two side lengths a and b. The distance between the coils is give by d.

In addition to the square Helmholtz coils, a cylindrical coil (Fig. 6) was constructed to test the capabilities of the PID controller. This cylindrical coil design can not be used for the actual stabilization in the experiment, because it has no free optical path to the center and the science chamber cannot physically fit inside. The exception is the one axis in which the field is generated. This free optical path also gets blocked if two other coils were added to compensate the other two directions. The three coil combination would also block physical access towards the inside of the configuration. Nevertheless one coil is used for testing purposes because it is easy to build and occupies not much space. The magnetic field in the center of such a coil is given by

$$\mathbf{B}(\mathbf{0}) = \mu_0 \frac{n\, I}{\sqrt{(2\, R)^2 + l^2}}, \tag{2.26}$$

with the current I, the number of turns n, the radius R and the height l [8].

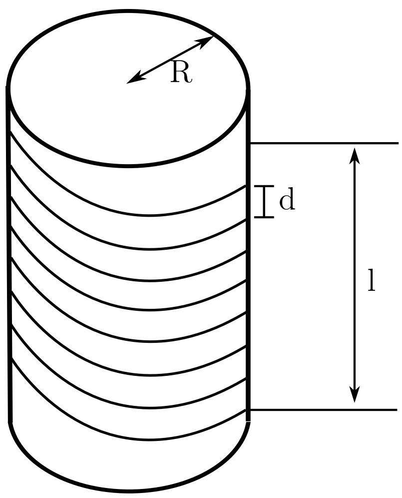

Figure 6: Cylindrical coil used for rapid testing of the PID. The dimensions are denoted as R for the radius, for the height l. The turns have an equal spacing of d.

2.1.3 Dynamic Characteristics of Coils

So far the focus was only on the production and shape of the magnetic field. This is not the only property of a coil configuration, the impedance Z is a second factor that has to be taken into account. It is the extension of the normal DC resistance of an electrical element at any frequency.
To determine this value, a bit of introduction is needed. The magnetic flux Ψ is defined as the integral over an area of the normal component of the magnetic field [8]. From this the definition of the magnetic induction L is possible with

$$\Psi = L\, I. \tag{2.27}$$

In this equation I represents the current. The next thing that is needed is Faraday's law [8]

$$U_{\text{ind}} = -\frac{\mathrm{d}}{\mathrm{d}t}\Psi. \tag{2.28}$$

In combination with Eqn. (2.27) and under the condition that L is constant, the induced voltage is dependent on the change of the current I. For the impedance Z, I is chosen to be sinusoidal, not only because most AC currents are sinusoidal, but also because this is the basis of the Fourier transform. The voltage looks then as follows

$$U = \frac{\mathrm{d}}{\mathrm{d}t}\left(L \cdot I\, e^{i\,\omega t}\right) = i\,\omega\, L \cdot I\, e^{i\,\omega t}. \tag{2.29}$$

Making use of Ohm's law, this can be transferred to the impedance. The commonly known resistance R is replaced with a the frequency dependent reactance $X_L(\omega)$,

$$X_L(\omega) = \frac{U}{I} = \frac{i\,\omega\, L \cdot I\, e^{i\,\omega t}}{I\, e^{i\,\omega t}} = i\,\omega\, L. \tag{2.30}$$

With this it is possible to make use of all the known rules for DC circuits. For example, a series connection of multiple impedance has the measured total impedance of the absolute value of the sum of all single impedance values

$$Z(\omega) = \left| \sum_i X_i(\omega) \right|. \tag{2.31}$$

As shown in Eqn. (2.30) the impedance for an inductor rises with increasing frequency. That means at high frequencies with the same amplitude of the voltage U the current amplitude I would be smaller, which directly leads to smaller amount of the induced magnetic field B, see Eqns. (2.21), (2.25) and (2.26).
If the PID controller changes the voltage with high frequency this loss in magnetic field will be noticeable and has to be taken into account by the controller. Another option to avoid this problem is not to use a voltage-controlled power supply (PSU), instead switch to a current-controlled one, because the magnetic field is linear to I. In this case the power supply takes care of supplying the right amount of voltage to the coils. The reason to use

this PSU regardless is that this one is the best one available, see Section 2.2.2 and can even be converted to a current-controlled one. The next better option is to use commercial current-controlled fast PSU, but their pricing is not reasonable for this project.
To get an estimate up to which frequencies the voltage-controlled PSU's are still good enough for a given inductance L, the so called 3 dB frequency is used. It is defined to be at the point where the power $P \propto I^2$ drops to the half of its starting value. One can confirm that

$$P_{\mathrm{dB}} = 10\,\log_{10}\left(\frac{P(\omega)}{P_0}\right) = 10\,\log_{10}\left(\frac{I(\omega)^2}{I_0^2}\right) = 20\log_{10}\left(\frac{I(\omega)}{I_0}\right). \tag{2.32}$$

The ratio of the current is near a value of $-3\,\mathrm{dB}$

$$\frac{I(\omega)}{I_0} = \frac{1}{\sqrt{2}}. \tag{2.33}$$

This is commonly just called 3 dB point. The next task is to find a theoretical expression of the inductance of the coil, or coil system. In most cases an analytical solution does not exist. An approximation can be made if the self inductance L_{self} of each coils is added to the mutual induction L_{self} to obtain the total inductance L [14]

$$L = 2L_{\mathrm{self}} + 2L_{\mathrm{mut}}. \tag{2.34}$$

The inductance of a square coil can be calculate again with an approximation [14] in Henries given by

$$L_{\mathrm{square}} = \frac{(1\cdot 10^{-5})\,(a/2)^2 n^2}{3a/2 + 9\beta + 10\gamma}, \tag{2.35}$$

where a is the diameter of the coils, β the axial cross section and γ the radial cross section. The last two values are normally very small compared to a. The mutual inductance can also be calculated with this formula and is given by [14]

$$2L_{\mathrm{mut}} = L_{\mathrm{square}}(a, d+\beta, \gamma) + L_{\mathrm{square}}(a, d-\beta, \gamma) - 2L_{\mathrm{square}}(a, d, \gamma). \tag{2.36}$$

The distance between two coils is given by d. Note that for thin coils $\beta \ll d$ the mutual inductance disappears.

For a circular loop the exact solution exists [7] and also for the cylindrical coil

$$L = n^2\,\frac{\mu_0}{4\pi}(2\pi\,R)\left[\ln\left(\frac{64/e^4\cdot R^2}{a^2} + \frac{1}{2}\right)\right] \approx \mu_0\left(\frac{n}{l}\right)^2 \pi\,R^2\,l, \tag{2.37}$$

where the cylindrical coil has the radius R and the number of turns n. The second equation is another simplification for long coils with $R \ll l$ with the length l [8].
This theory assumes that the coils is ideal, in reality a wire, an inductor, also has a resistance and a capacitance.

2.2 Coil Layout and Simulation

With the knowledge gained in Section 2.1 the coils dimensions and layout can be defined. For the PID testing a cylindrical coil was chosen. For the final goal to stabilise the magnetic field in all three directions the decision was made to use a square Helmholtz coil, due to space constraints, building options and optical access (See Section 2.1.2).

2.2.1 Magnetic Field

The first and most important thing to consider is the capability of the coils to generate an appropriate **B** field. Therefore the magnetic field was measured for a time span of about 5 s to see the fluctuations that occur. This result gives a good impressions of the fast change in magnetic field, but is not enough to get a full idea of the occurring fluctuations. A longer measurement is needed to see small drifts over the day, which should be ideally also suppressed. These two data sets can be found in Fig. 7.

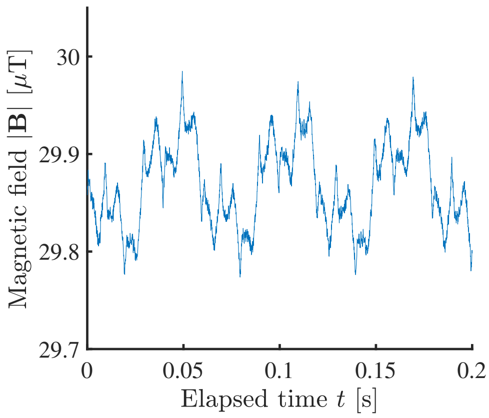

(a) Short time span.

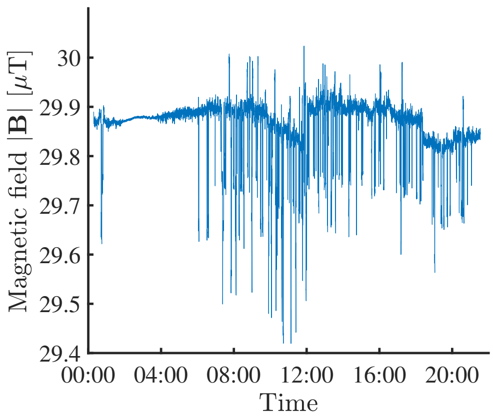

(b) Long term measurement.

Figure 7: Fast and slow changes of the magnetic field over nearly a complete work day. The measurement is staring at 0:30 and ending at 21:30.

The maximum amplitude of the fast fluctuations is at 0.2 μT and at the long term drift look very stable with a maximum peak to peak value of 0.6 μT. It is visible that at night the signal is very stable. At around 4:00 the signal gets more noisy. This time corresponds with the time at which the first trains are scheduled. At around 6:00 the first major peaks start to appear. That is the time at which the first people enter the building and starting their experiments. At lunchtime 12:15 the magnetic field shows a sudden increase. In addition to the peak to peak value of the magnetic field it is advisable to pick a buffer that can compensate for unforeseen drifts. In this case it was set to 10 times the minimum requirement and so has to be greater than 6 μT. It is also important to not exceed this value by far, because then the noise of the control voltage translates to a greater noise of the **B** field.

The second important fact that has to be taken into account is the capability of the power

supply to provide enough current to the system. The PSU used was a power amplifier mounted on a development board, the OPA548EVM . Its maximum possible continuous current of the OPA548EVM is 3 A [15], but the evaluation board is limited by its cooling capabilities. In our tests currents up to 2 A can be handled over a longer time without a huge cooling effort. If the current has to be pushed beyond this limit a cooling fan increases this limit up to circa 3 A.
The last constraint to the coils was the building space. The originally designed μ-metal shield has a side length of 55.9 cm on its smallest side. Due to the fact that the science chamber is not in the middle of this shield the 60 cm are not a valid choice for a symmetrical alignment (see Fig. 8).

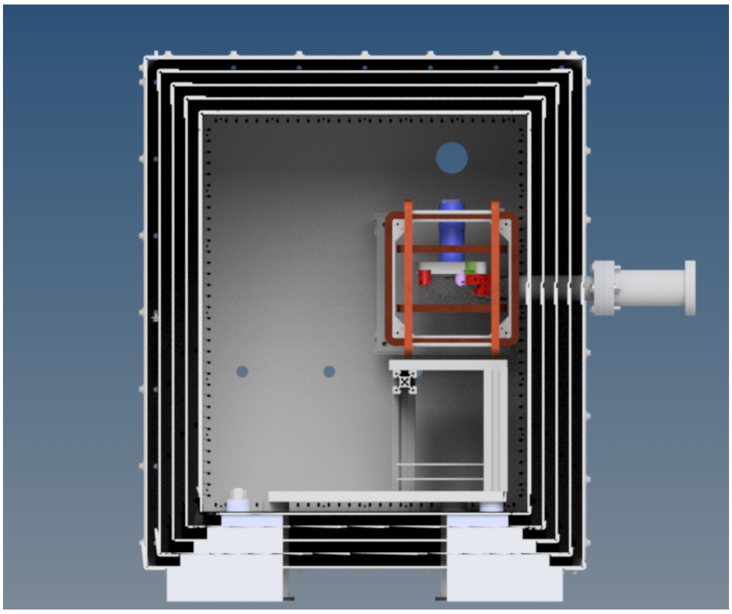

Figure 8: Location of the science chamber along with the science cell coils inside the μ-metal shield. With this design, coils would produce gradients of components of the field of approximately 200 nT/mm A in the most affected directions. Gradients need to 12 nT/mm A at 5 A coil currents. The stabilization coils would replace the shield, while not exceeding the boundaries of the initial design.

Based on the corresponding CAD drawings the maximum side length was around 40 cm. Larger coils create an also larger area where the magnetic field is homogeneous. In general it is a good idea to choose a large coil distance, this leads to a greater homogeneous region of the magnetic field. If the sensor is not perfectly centered in the coils the measure field would have then a smaller difference from the center. The reason not to go with the full width of 40 cm was the practical option to mount these coils on an optical table. Optical tables have screw holes every 2.5 cm, so if the holes on the three dimensional coils system are next to the X intersection (see Fig. 12) than this length has to be a multiple of the 2.5 cm spacing. This leads with the optimal distance of $d = 0.5445\,a = 20\,\text{cm}$ to side length of

$$a = 36.7\,\text{cm}. \tag{2.38}$$

This result is the closest to 40 cm possible under the given spacial constraints. The special characteristic of the planned coils is that they should have all the same properties. Specially, the coils have the same number of windings n and side length a, in addition to a symmetrical alignment. For the realization see Section 2.2.3. The only variable now left is the number of turns. It was chosen to be

$$n = 3, \tag{2.39}$$

because with this value it could achieve the given requirement of the magnetic field. It is capable of producing

$$\frac{B}{I} = 13.30\,\mu\mathrm{T/A} = 133.0\,\mathrm{mG/A} \tag{2.40}$$

in the center. The final dimensions are summarized in Tab. 1.

Description	Parameter	Value
Side length	a	36.7 cm
Coil spacing	d	20.0 cm
Number of turns	n	3

Table 1: Parameters used for building the three square Helmholtz coils.

An old set of square coils, built by Matthias Wenzel in his Bachelor thesis 2012 [16], was also available. These coils fulfill not the requirements given in Section 2. The dimensions are stated in Tab. 2, because it was also tested in this thesis to see the impact of purpose-designed coils compared to a non–optimal one.

Description	Parameter	x coil	y coil	z coil
Side length	a	42.1 cm	22.5 cm	17.4 cm
Side length	b	21.7 cm	22.5 cm	17.4 cm
Coil spacing	d	13.0 cm	17.8 cm	19.0 cm
Number of turns	n	40	40	40

Table 2: Measured dimensions for each one of the old rectangular coil system.

The second type of coil, the cylindrical one, has to deal with the same first two properties. They have to compensate a field of $6\,\mu$T with a maximum current 2 A. This was in this case no problem, the reason to make these coils a little bit stronger was a geometrical one. The number of winding was reduced to a absolute minimum of $n = 10$, while still having a decent number of turns per height increase. The final parameters are listed in Tab. 3 and with these values it is able to produce in the center

$$\frac{B}{I} = 107.76\,\mu\mathrm{T/A} = 1077.6\,\mathrm{mG/A}. \tag{2.41}$$

Description	Parameter	Value
Height	l	10.0 cm
Diameter	d	5.0 cm
Number of turns	n	10

Table 3: Parameters for the used cylindrical coil.

2.2.2 Impedance and Frequency Response

The next important property to consider is the impedance. The general concept of this was already discussed in the theory sections, Section 2.1.3. But before the impedance design for the coils is discussed another crucial part of the system is examined, the power supply. In Section 2.1.3 it was explained why a current-controlled power supply would improve the issue of a rising resistance of a coils with increasing frequency. The current-controlled PSU that was available was the EA-PS 3016-20 B from Elektro-Automatik, in the following only referred as EA-PS . The specification of this component are that it can supply a voltage of 16 V and a current up to 20 A. So it looks like it should be more than enough buffer to drive the coils to the required limits, Section 2.2.1. The problem with this specific power supply comes from its frequency response, it is stated in the data sheet to a rise time 10 % to 90 % of the load in under 1 ms. This leads in a direct conversion to a frequency of 1 kHz. This can be tested in an experiment. The experimental setup is shown in Fig. 9. To measure the frequency response of the EA-PS the connections A and B are shorted and the corresponding PSU was chosen.

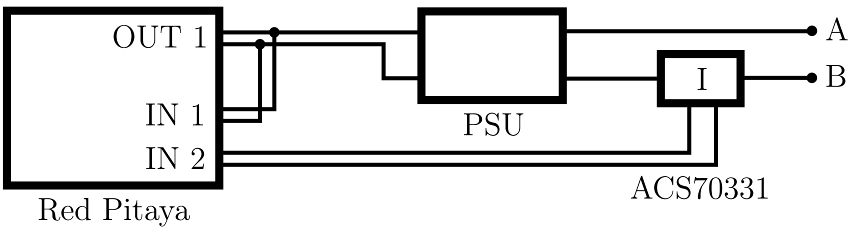

Figure 9: Experimental setup to measure the frequency response of a system connected to A and B.

In this experiment the PSU was given a sinusoidal input signal with a fixed frequency f that is generated by Red Pitaya. This signal and the output current I of the PSU were measured by this Red Pitaya. The used current sensor was based on the giant magnetoresistance technology and called ACS70331 from Allegro MicroSystems. If the current is 0 A then the output voltage is at 1.5 V, it changes its output voltage about 0.4 V/A in a range of 0 V to 3.3 V. After one measurement is completed, the data t and $I(t)$ is saved and the frequency is changed to the next one. With this measurement random sampling was used to compensate the error that occurs due to thermal heating. For this part the total possible error is not that important, because this measurement is only a test of the frequency response of the PSU. If its 3 dB point is roughly in the range of interest then this PSU in not suitable for this applications, so even if the error suggest that it could be used at a slightly higher frequency this would not change its 3 dB point drastically. The measured data is displayed in Fig. 10. The second PSU was a power amplifier, the OPA548. This one was introduce in Section 2.2.1. The same measurement as with the EA-PS as conducted with this one, compare Fig. 9. The results are also shown in Fig. 10.

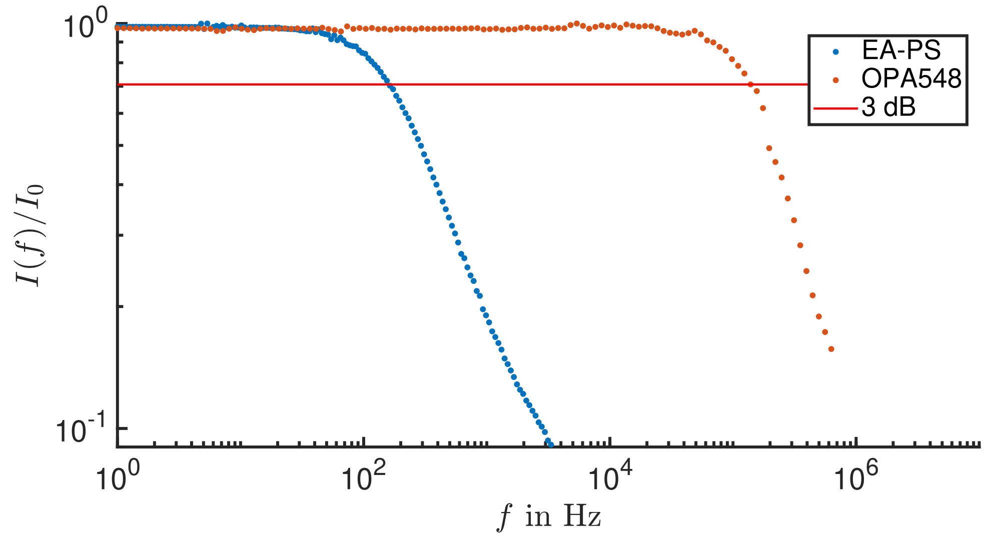

Figure 10: Frequency response of the two power supplies EA-PS and the OPA548. The OPA548 has a much higher 3 dB frequency due to its simple, but fast design.

In this plot the ratio of the root mean square of the current $I(f)$ at the specific frequency f and the root means square value of $I(0\,\text{Hz})$ at 0 Hz. Taking a look at the data of the EA-PS it is visible that its 3 dB point, marked by the red line, is around 160 Hz. This value is not even close to the desired frequency, the magnetic sensor FLC3-70, that will be introduced in Section 3.2, is capable of measuring the $\mathbf{B}$ field up to frequencies of 1 kHz. In comparison looking at the data of the OPA548, its 3 dB point is much higher at around 140 kHz and exceeds the limit given by magnetic sensor by far.
From this results the choice to use the OPA548 was made. The drawback of this PSU is that is, as shipped, a voltage-controlled PSU, so more thoughts have to go into the impedance design of the coils. To give a small outlook, the best option to drive coils is a so called four-quadrant signal amplifier. This can be seen as a normal current-controlled PSU, but the difference is the four-quadrant term. The EA-PS can be seen as an one quadrant signal amplifier, because it can only supply positive current. A two quadrant amplifier can normally supply positive as well as negative current. The other two quadrants are for sinking power, this is useful for coils, because they can store energy in their magnetic field and if the field is reduce quick then this energy has to go somewhere else. The four quadrant sink this power and are due to this reason faster.
The equations given in Section 2.2.2 are the main guidelines to pick coil dimensions, but the magnetic field has still priority. That is why the the square Helmholtz coils have this huge inner diameter, because it produces a large area of a homogeneous field, even though it increases the inductance. The number of turns n increases the inductance quadratically, so it is useful to take a low number. This collaborates with the goal to not produce too

large magnetic fields (see Section 2.2.1). The old square coils could not be manipulated, they have a number of turns of $n = 40$ and so they have a higher inductance, even though they are smaller than the new square Helmholtz coils.
Nevertheless all of the coils have a finite impedance, which can not be neglected if a voltage contolled power supply is used. A method to compensate this behaviour is to add a resistor to the coils. This approach seems first counterintuitive because normally the goal is to make the resistance R of coils as low as possible. With a higher resistance the power loss will be greater at the same current I,

$$P = R\,I^2 \tag{2.42}$$

and so more heat is produced. In Fig. 11 this approach is graphically explained.

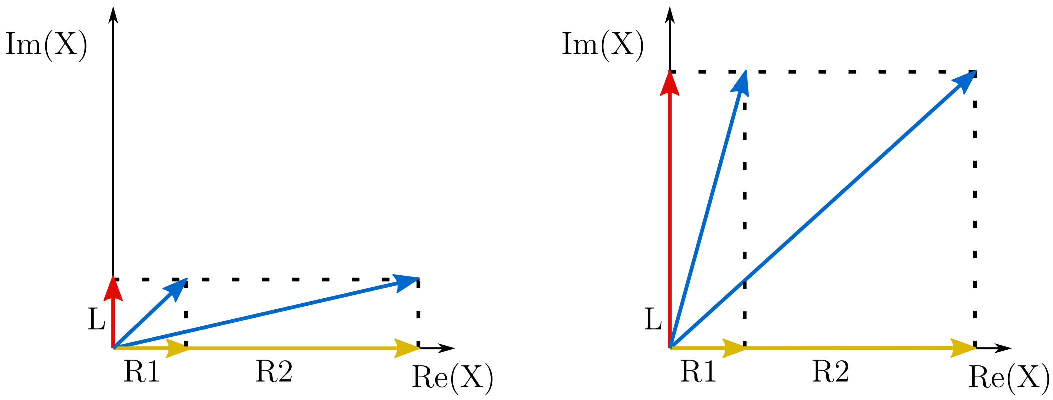

(a) Low AC frequency. (b) High AC frequency.

Figure 11: Total impedance X, represented by the blue arrow, at two different frequencies of system containing a coil and a low/high resistance. The red arrow represents the inductance value of the coils, the yellow counterpart resembles the resistor value.

The real part of X stays at all frequencies the same, because the only contribute to this, is the resistance R which is constant. The imaginary part of the impedance $\mathrm{Im}(X)$ rises linear with frequency as shown in Eqn. (2.30). The total impedance is the absolute value of the sum of all single contributors. In the case of a high constant R the impact of a small changing imaginary part contributes not that much to the total X as it would with a lower resistance. This is trivial and can be verified just by looking at Figs. 11a and 11b.

2.2.3 Building the Magnetic Coil System

This was the theory and planning, the next step is of course the building which includes an implementation of the required features. To give the wire the desired shape, a guiding structure is needed. The way to go is to use U-shaped profiles which hold the wire inside. The used material was aluminium, because of its magnetic susceptibility of $\mu_r = 1 + 2.3 \times 10^{-5}$ [8]. For the wire a litz wire with the diameter of 2 mm is used, it consist

of multiple small isolated single wires which are combined to a bigger one surrounded by a fabric hull. The reason to choose this wire, was not its good high frequency capabilities, because only frequencies up to 1 kHz are applied, it was its good capability to bend around corners easily. In Section 2.2.1 the number of turns was set to be $n = 3$, a wire diameter of 2 mm leads to a total length of 6 mm if the wires lie next to each other. The inner diameter of the U-profiles was because of this also set to 6 mm, which was possible because the litz wire can be a squeezed a little bit, due to its multiple small wires, and fits after that perfectly in the rail.
The next step is to design the connection of the profiles. The first thought is to not use a complete connected metal loop for the U-profiles that hold the wires in place. If they are connected like this common way, compare with to the old coils that are available, it is possible that a current can be induced in these loops and distort the intended field. The solution for this problem is to use at the corners of a loop connectors that are non conducting. In this case the choice is made to use 3D printed L-connectors, Fig. 12 made out of PLA. They have good material properties, they are non conducting up to a limit where it is not important anymore, the magnetic susceptibility is close to 1 [9] and the important fact is the easy manufacturing of this material. It exist a lot more material option, that fulfill the first two requirements, for example PEEK is a very good material for this purpose. It is a little more reliant than PLA, but, and that is important, it has to manufactured in a workshop where they CNC milling machine. On the other hand PLA can be printed which makes it perfect for rapid prototyping, if a part breaks then another one can be printed quickly. It only takes around 30 minutes up to 1 hour. The total production time is shorter than given an order to a busy workshop where it has to wait a longer time. For all parts it took only one week of printing on two printers, with all the additional no operating time that can not be avoided.

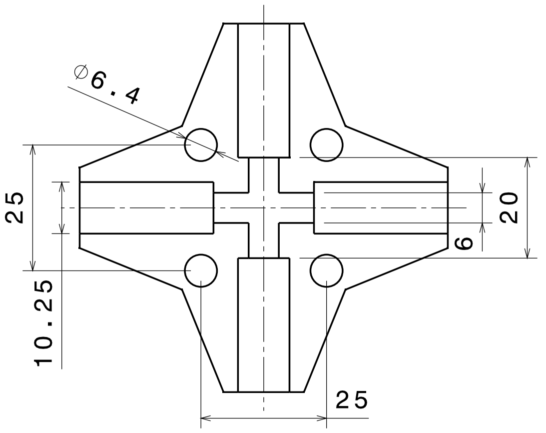

(a) Drawing X Mount.

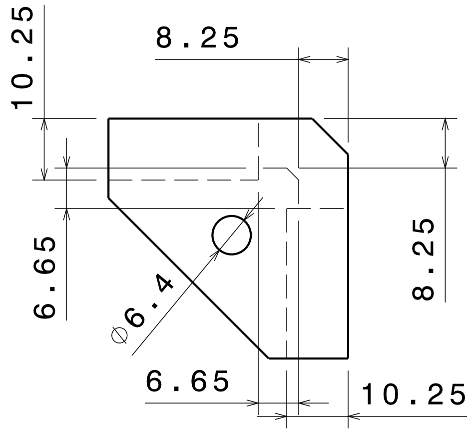

(b) Drawing L Mount.

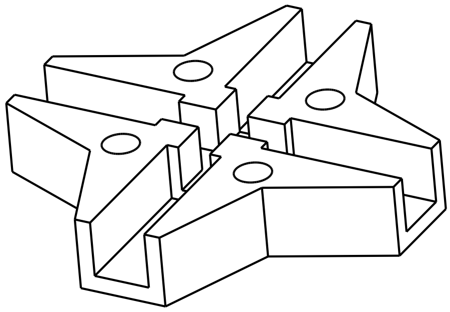

(c) Isometric view X Mount.

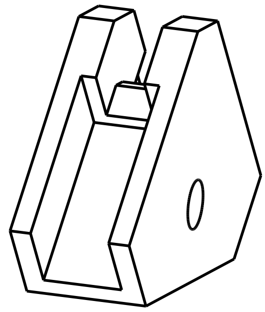

(d) Isometric view L Mount.

Figure 12: L- and X-connectors used to connect the aluminium U-profiles of the coil cage. The non conductive nature of PLA also permits induced loop currents to flow through the cage.

The second challenge is to make all coils equal in diameter and mount them symmetrically. This provides a system in which all three dimensions are similar and have the same properties. It will make it easier to built and tune a controller for stabilisation. If a conventional method is chosen than only one of this requirements can be fulfilled. If they are mounted with a common center point, they have to have a different diameter because otherwise the aluminium profiles would collide with each other. If they have the same diameter they have to be shifted in different directions to avoid the same problem. To solve this issue, the profiles are cut at their point of collision and a X-connector, Fig. 12, is inserted.
The third thing that has to be considered is the capability to mount the coils on to an optical table. This was already mentioned in Section 2.2.1. The distance between the X-connectors has to be a multiple of the distance between the screw holes on the table. The best distance was $d = 20\,\text{cm}$, which leads to the odd total diameter $a = 36.73\,\text{cm}$. The length of the aluminium profiles has to be adjusted to fit these dimensions. In Tab. 4 the length and the amount of every component is listed. If one carefully adds up all

lengths in one direction

$$L = (6.65 + 66 + 20 + 180 + 20 + 66 + 6.65)\,\mathrm{mm} = 365.3\,\mathrm{mm} \tag{2.43}$$

it is visible that this value is 2 mm to short to hit the desired 367.3 mm. This is done on purpose, because the wire has a diameter of 2 mm and is not stacked. An amount of 1 mm has to addend at each side to reach the center of the wire, at which the current can be centralized if has a radial symmetric current density in the wire.

Component	Length	Amount
L-connector	—	24
X-connector	—	24
U-profile	180 mm	24
L-profile	66 mm	48
Litz wire	ca. 5 m	6

Table 4: List of components for the 3D square Helmholtz coils.

The profiles are glued to the connectors, because it was not possible to fit a screw in the design without using a unreasonably huge aluminium profile, or make proper winding the coils impossible. The ending of each loop are twisted and taken away in a straight line to create minimal distortion to the magnetic field. Because of the small number of turns an additional wire with the same current close to the coils in not optimized position would have a relatively high impact on the generated magnetic field. The final build is shown in Fig. 13. As a side note the building process and the final result, was exactly as planned in the theory, also the field fits exactly the expected one, see Section 2.3.3. For later projects this method is highly recommended.

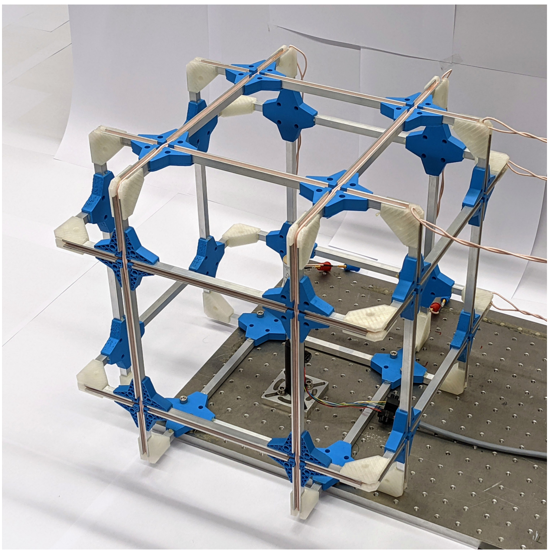

Figure 13: Picture of the final square Helmholtz coils used to generate and stabilise the magnetic field. The coil system is mounted on an optical bread board to provide good alignment for the magnetic field sensor, seen behind an aluminum profile in the middle of the coils.

The second coil build, had a cylindrical shape, the easiest method to produce an accurate representation of the theory is to also print a guiding shape on which the wire sits. Due to the large distance in z direction into the cylinder a notch is inserted to ensure the perfect geometry of the wire. In this case it was not necessary to use litz wire because the curvature of the wire was not as tight as it would be with corners present. A press fit also has not be done due to the single wire at one place which can be glued into the perfectly spaced notch. So the used wire was a normal isolated copper wire with a diameter of 2 mm. The final result is shown in Fig. 14.

Figure 14: Picture of the cylindrical coil used for testing.

2.3 Experimental Test and Results

This section discusses the results of the available coils and compares it to the previous theory. It also picks the up the arguments in favour or against specific coils, that are made in Section 2.2.

2.3.1 Old Coils

The first results will be the one of the old coils, that were available and used in a previous experiment. This configuration consist of three different sized coils, see Tab. 2. Due to the high number of turns and the small diameter of the wire, resistance is high enough that it can be measured with a multi meter. This is especially for small resistances a not highly accurate method, which has to be kept in mind in further calculations. The measured resistance of the coil plus the current sensor, Fig. 9 is stated in Tab. 5.

Coil	R [Ω]	L_{theo} [mH]	L [mH]	α [μ H^2/Ω^2]
x	8.5(2)	1.2	9.5(3)	7.8(5)
y	6.1(2)	0.84	6.0(2)	6.0(5)
z	0.6(1)	0.49	1.9(1)	60(4)

Table 5: Measured resistance R and calculated impedance L_{theo}. The impedance L is determined through the fitting parameter α of the function $F(f) = 1/\sqrt{1+\alpha f^2}$ for the normalized frequency response.

The theoretical inductance of the coils is given by Eqn. (2.36) and also written in Tab. 5. The data in Fig. 15 is recorded the same way as the frequency response of the power supplies is done, with the corresponding coil connected to A and B (see Fig. 9). The faster PSU, the OPA548, was used to have a minimal influence of the frequency response of the PSU to the result. That this assumption holds is directly visible in Fig. 15, because the OPA548 has a 3 dB frequency of 140 kHz.

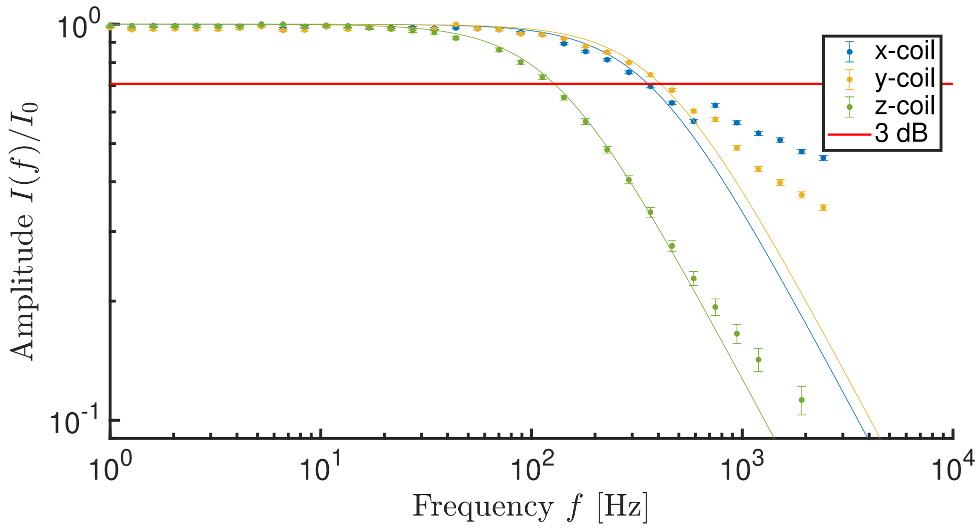

Figure 15: Frequency response of the three old coils in addition to a fit $F(f) = 1/\sqrt{1+\alpha f^2}$ to determine the inductance over the resistance. The error is determined through the standard deviation of the signal at low frequencies where the curve is linear.

The error bars in this plot is determined form the deviation of the measurements at low frequencies where the amplitude in approximately constant. The fit function does not matches exactly the experimental data at every frequency and deviates from the fit. A possible reason for this is that the resistance is not constant and could change at higher frequencies. Also parasitic capacitance or the PSU coil combination could lead to a different shape. The last one is related to the used wire and indeed the x, y coils are made of a different type then the z coil which deviate less. The determined impedance L is stated in Tab. 5 along side with the theoretical one. These corresponding values are not the same, even with the stated error, which is related to the error of the measured resistance and the error of the fit parameter. One of the reasons is that the measured

parameters for the coils are wrong. The coils have not of the most accurate design. For example the z coils are only held in place by cable straps. The more important observations are the real 3 dB points of all coils. The frequency at this point is at 350 Hz for the x coil system, for the y coils at 420 Hz. The z coils have a especially low 3 dB frequency of 125 Hz, because they have a low resistance due to thicker wire. All of the frequencies are too low to be valid up to the 1 kHz limit of the sensor, which is one of the reason to build new coils. This results shows the importance of the resistance if a voltage-controlled PSU is used.
The magnetic field is the second measurement. It was not introduced yet and so needs an introduction, the schematic is shown in Fig. 16.

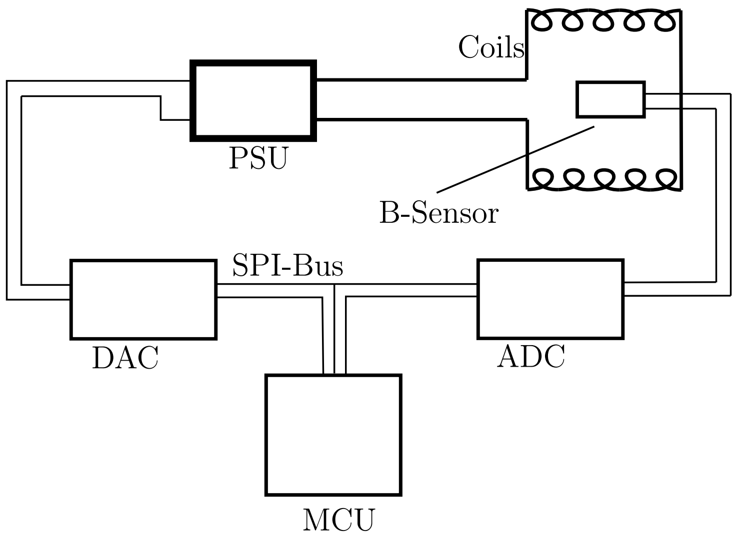

Figure 16: Experimental setup to measure the generated magnetic field of different coils. The microcontroller (MCU) is the central control unit, which reads the magnetic field (of the B-Sensor) with an analog to digital converter (ADC). The output voltage that controls the power supply (PSU) is generated by an digital to analog converter (DAC).

The setup uses an digital to analog converter, the DAC81408 from Texas Instruments, to write a voltage to the PSU. All components, with their important specifications are introduced in Section 3.2. The power supply is not the fast OPA548, but it is the EA-PS, due to its current control mode. It is convenient that with this a current can be produced more precisely than with a voltage controlled one. This PSU compensates the change of the resistance that comes for example due to the impedance or, and this is more important, due to heating of the wire while the measurements are done. This effect is also compensated due to arrange the measurement points in an random order. The actual field is measured with the FLC3-70 sensor, see Section 3.2,which produces a voltage that is again measured with an analog to digital converter the AD4111. To minimise the error of the magnetic field value the measurement was done multiple times $n = 1000$, this compensates both the statistical noise error of the ADC and the surrounding magnetic field oscillation. The resulting error is so small that writing it into Fig. 17 would only make each point harder to read with no real benefit. The error bar in the the current I

direction is way larger, because the noise of the voltage output of the DAC is at $20\,\mathrm{mV_{pp}}$ which translates to a $40\,\mathrm{mA_{pp}}$. The error of the EA-PS is negligible with $4\,\mathrm{mA_{pp}}$[17]. In this experiment the magnetic field only in the intended direction of the coils is measured, because in the center point this should be the only generated one. The magnetic field in Fig. 17 at zero current is set to zero to only measure the produced magnetic field.

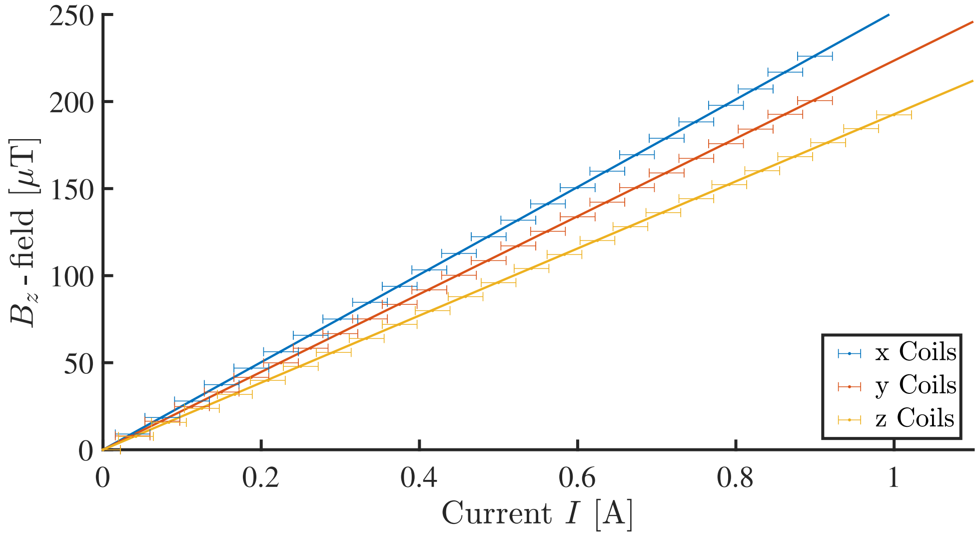

Figure 17: Magnetic field generated by each coil, measured in the direction of the alignment of the coils, with a linear fit $B(I) = \alpha\, I$.

The fit parameters are stated in Tab. 6 in comparsion ti the theoretical derived values from Eqn. (2.25) with the used parameters Tab. 2.

Coil	$(B/I)_{\text{theo}}$		B/I	
	[μT/A]	[mG/A]	[μT/A]	[mG/A]
x	247.36	2473.6	251.54(8)	2515.4(8)
y	215.93	2159.3	223.53(8)	2235.3(8)
z	187.80	1878.0	192.72(5)	1927.2(5)

Table 6: Fitted values of for the magnetic field per current B/I, in comparison with the predicted values. The sated error is obtained from the deviation of the fit.

This theory fits a lot better than the impedance calculations for this coils. But there is still some deviation of the actual values from the theory, that could have multiple issues. The size of the error bars is already mentioned, but in those the error of the theory is not taken into account. This error comes mainly from the uncertainty of each parameter that is used. This coils have, as already said, not the cleanest design. The windings are not always parallel and are denser at some sections, especial at the y coils. The z coils have very loose turns which leads to a cross section that is not close to the intended square shape and becomes more like a round one. The next worst thing of this specific pair is that the two coils are held in place by cable straps. This produces neither a good

alignment in x and y direction and no a fixed rotation against each other.
This result shows also that these coils, as expected in Section 2, are not well suited. Every axis has a different magnetic field per current, which makes it a lot harder for the PID, and especially for the tuning, see Section 3.3. The amount of B/I also exceeds the required limits by far, which will leads to problems, and would require an even more precise control voltage for the current modulation.

2.3.2 Cylindrical Coils

Before a similar plot as Fig. 15 can be produced the resistance of the cylindrical coils has to be determined first. The quick method to use a multi meter to measure the resistance fails, because $R_0 < 1\,\Omega$. To get however an estimate of the value a simple circuit, Fig. 18, can be used.

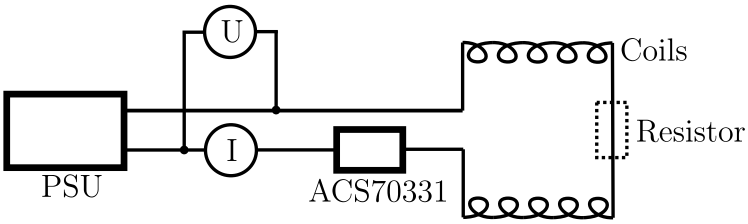

Figure 18: Experimental setup to measure the resistance of the setup, consisting of the current measurement component ACS70331, the coils and eventually a $1\,\Omega$ resistor. The current is delivered by a power supply PSU and measured by two multi meters U and I.

This makes use of two multi meters, one measures the current the other one the voltage. The current is increased in multiple steps, where at each both values, the current and the voltage, are recorded. From this results the resistance of the whole loop can be calculated. All values are found in Tab. 7, the last line is the average of the resistance. The important thing to keep in mind is that the resistance of the ACS70331 R_{ACS} and the one of the multi meter R_{MM}, which is performing the current measurement, is also included in this value. The resistance of the first one is important and correct to measure this one too, because this component is also in the frequency response measurement. The multi meter will not be in this measurement, compare Fig. 9, and has to be excluded. This is done by only measuring its resistance and subtracting it from the final result.

$R_L + R_{\mathrm{ACS}} + R_{\mathrm{MM}}$			$R_{1\,\Omega} + R_{\mathrm{MM}}$		
U [V]	I [A]	R [Ω]	U [V]	I [A]	R [Ω]
0.045(3)	0.29(1)	0.155(15)	0.443(7)	0.399(7)	1.11(4)
0.118(4)	0.78(1)	0.157(7)	0.81(1)	0.74(1)	1.10(3)
0.155(4)	0.98(1)	0.158(6)	1.15(1)	1.04(1)	1.11(3)
0.204(5)	1.29(2)	0.157(5)	1.38(1)	1.25(2)	1.10(2)
0.245(5)	1.56(2)	0.158(5)	1.60(2)	1.45(2)	1.10(2)
0.287(5)	1.82(2)	0.157(5)	1.971(2)	1.79(2)	1.10(2)
0.325(6)	2.06(2)	0.158(5)	2.27(2)	2.06(2)	1.10(2)
0.376(6)	2.38(3)	0.158(4)	2.60(2)	2.36(3)	1.10(2)
0.433(6)	2.75(3)	0.158(4)	3.04(3)	2.76(3)	1.10(2)
0.492(7)	3.12(3)	0.158(4)	3.38(3)	3.06(3)	1.10(2)
		0.157(1)			1.10(1)

R_{MM}		
U [V]	I [A]	R [Ω]
0.058(3)	0.75(1)	0.077(6)
0.083(4)	1.07(1)	0.077(4)
0.114(4)	1.47(2)	0.077(4)
0.139(4)	1.74(2)	0.080(3)
0.155(4)	2.09(2)	0.074(3)
0.190(5)	2.587(3)	0.073(3)
0.201(5)	2.755(3)	0.073(2)
0.233(5)	3.216(4)	0.072(2)
0.290(5)	4.005(4)	0.072(2)
0.315(6)	4.383(5)	0.072(2)
		0.075(1)

Table 7: Measured current I and voltage R of different combinations to determine the resistance of the coils R_L + ACS70331 R_{ACS} and of the used $1\,\Omega$ resistor $R_{1\,\Omega}$. The resistance of the multi meter R_{MM} is also measured to be later subtracted. The error is set to the least significant digit because the statistical error was smaller that the last digit.

The resistance of the coils and the sensor ACS70331 is according to this data

$$R_0 = 0.157(1)\,\Omega - 0.075(1)\,\Omega = 0.082(2)\,\Omega, \tag{2.44}$$

if the used $1\,\Omega$ resistor is added the total resistance increases to

$$R_1 = R_0 + (1.10(1)\,\Omega - 0.075(1)\,\Omega) = 1.11(1)\,\Omega. \tag{2.45}$$

These two values can be used, with Eqn. (2.37) to calculate a theoretical inductance L_{theo} similar to Section 2.3.1. A fit along with the experimental data is shown in Fig. 19, which is recorded in the same way as for the old coils (see Section 2.3.1).

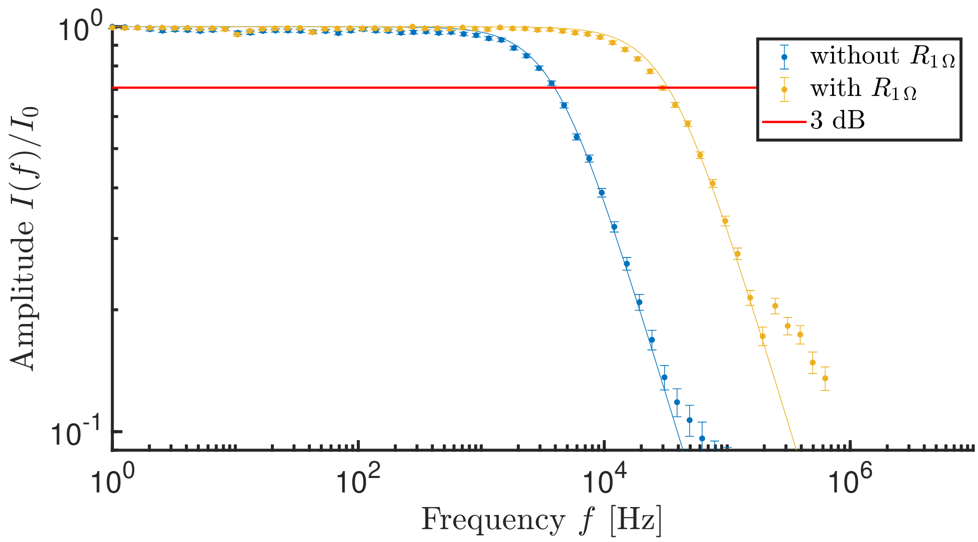

Figure 19: Frequency response of the cylindrical coils, with and without an additional $1\,\Omega$ resistor $R_{1\,\Omega}$, in addition to a fit of $F(f) = 1/\sqrt{1+\alpha\, f^2}$. The error is determined through the standard deviation of the signal at low frequencies where the curve is linear.

This plot shows that this coil is way better suited than the old coils. In comparison with the old coils which had 3 dB points at 125 Hz, 350 Hz and 420 Hz, the critical point of this coil is at 4 kHz without $R_{1\,\Omega}$ and at 32 kHz with $R_{1\,\Omega}$. Its 3 dB frequency even without the additional resistor is good enough that the coil can be driven at frequencies at 1 kHz with no big impact of a higher impedance. The reason to use the resistor nevertheless is that it increases the accuracy of the supplied current. Due to the voltage-controlled power supply a small change in the input voltage, could be noise, will change the current/magnetic field more if the resistance is lower.

Type	R [Ω]	L_{theo} [μH]	L [μH]	α [$n\,\text{H}^2/\Omega^2$]
without $R_{1\,\Omega}$	0.082(2)	9.87	8.3(4)	64(3)
with $R_{1\,\Omega}$	1.11(1)	9.87	13.4(5)	0.92(5)

Table 8: Determined resistance R and calculated impedance L_{theo}. The impedance L is determined through the fitting parameter α of the function $F(f) = 1/\sqrt{1+\alpha\, f^2}$ for the normalized frequency response.

The average of the the inductance is $L = 10.9\,\mu$H this value is closer to the theoretic model than it is the case for the old coils. This value is still not so close that the 3 dB point can be precisely determined from this. One conclusion is that theoretical impedance calculation, with only a theoretical model and a measured resistance is not always accurate. The important thing is to actually measure the frequency response of the system, which 3 dB should lie roughly at the same order as the planned one.
The generated magnetic field on the other hand, corresponds similar to previous chapter

good with the theory. In this case the measured data fits exactly the theory, because the coils are designed and build in a more precise way, which is helped also caused by the less number of turns. A notch with the right width and length is printed in a cylinder with the right radius to hold the wire. In addition to this the printed mount for the sensor gives extra accuracy of its placement in the center. With this the result in Fig. 20 is possible. The linear fit result $\alpha = B/I$ gives a value of

$$B/I = 107(4)\,\mu\mathrm{T}/A = 1070(40)\,\mathrm{mG}/A \tag{2.46}$$

for the magnetic field per current. The error is given by a maximal/minimal possible fit in range of the error bars. This value is close to the theoretical value of

$$(B/I)_{\mathrm{theo}} = 107.8\,\mu\mathrm{T}/A = 1078\,\mathrm{mG}/A. \tag{2.47}$$

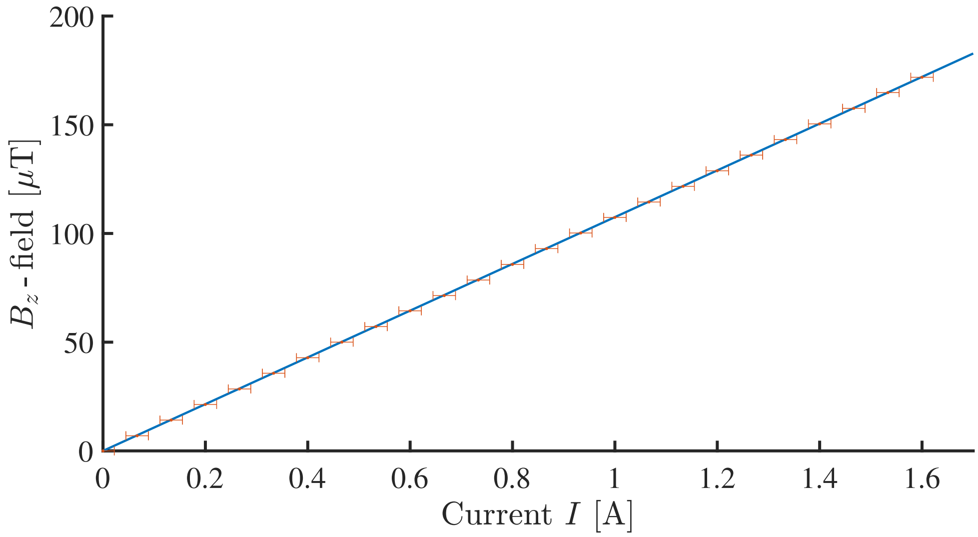

Figure 20: Measured magnetic field B_z generated by the cylindrical coil, measured in the direction of the alignment of the coils. The current was sampeled random and the data fitted with $B(I) = \alpha\, I$.

2.3.3 Final Coils

To measure the frequency response the resistance of the coils has to be also determined first. For this the same setup, as in Section 2.3.2, with the same multi meter and the same resistance was used. The schematic is given in Fig. 9. The only new measurement that has to taken is the measurement of the resistance value of the coils, because all other components are the same and have the same value. For the frequency response only the z coils are a reviewed, because all coils have the same geometry and therefore should have the same properties. To verify that every coil was not damaged during the building process the magnetic field of each is reviewed later. The resistance of the z coils is calculated from the values found in Tab. 9.

U [V]	I [A]	R [Ω]
0.090(4)	0.381(7)	0.236(14)
0.158(4)	0.67(1)	0.236(10)
0.205(5)	0.87(1)	0.235(8)
0.251(5)	1.07(1)	0.235(8)
0.294(5)	1.25(2)	0.235(7)
0.364(6)	1.550(2)	0.235(7)
0.406(6)	1.730(2)	0.235(6)
0.490(7)	2.088(2)	0.235(6)
0.565(8)	2.404(3)	0.235(6)
0.631(8)	2.685(3)	0.235(6)
		0.235(1)

Table 9: Measured current and voltage of different combinations to determine the resistance of the final z coil. The final line is the average result of R.

This leads to a resistance for the coils of

$$R_0 = 0.235(1)\,\Omega - 0.075(1)\,\Omega = 0.160(2)\,\Omega \tag{2.48}$$

with out the resistor and

$$R_1 = R_0 + (1.10(1)\,\Omega - 0.075(1)\,\Omega) = 1.19(1)\,\Omega \tag{2.49}$$

with the resistor. This can be used for the impedance calculation with the value for the inductance calculated with Eqn. (2.36). The results are shown in Fig. 21.

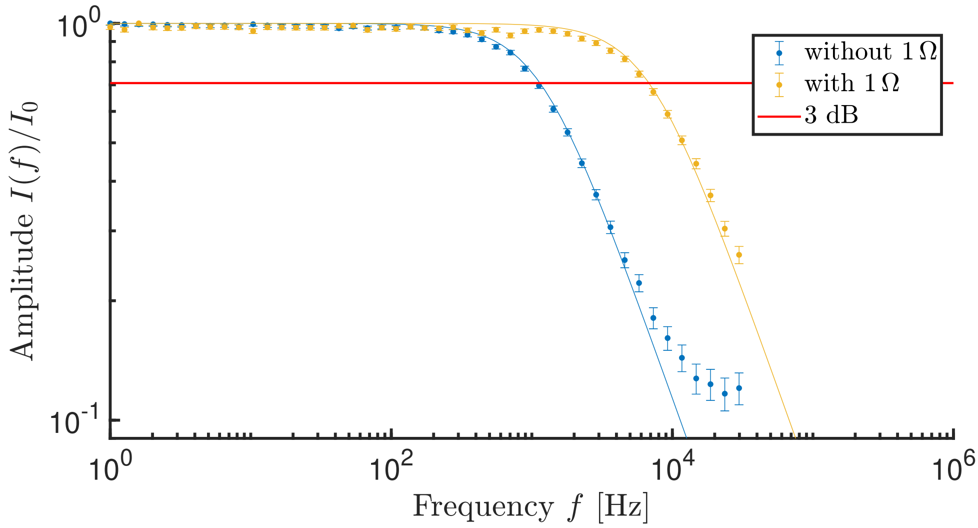

Figure 21: Frequency response of the final z coils, with and without an additional $1\,\Omega$ resistor $R_{1\,\Omega}$, in addition to a fit of $F(f) = 1/\sqrt{1 + \alpha\, f^2}$. The error is determined through the standard deviation of the signal at low frequencies where the curve is linear.

As in all frequency plots the theory is a bit off, but the general result is at the same order. The fitting parameter α obtained from the plot is along side the calculated results and the theory values in Tab. 10.

Type	R [Ω]	L_{theo} [μH]	L [μH]	α [$\mu\,\text{H}^2/\Omega^2$]
without $R_{1\,\Omega}$	0.160(2)	63	56(2)	0.77(4)
with $R_{1\,\Omega}$	1.19(1)	63	70(3)	0.021(1)

Table 10: Fitted parameter α of the fit function $F(f) = 1/\sqrt{1+\alpha\, f^2}$ to the normalized frequency response of the z coils. Along side is determined resistance R and calculated impedance L_{theo}.

The important fact is that the coils with or without the resistor are good enough to use them with frequencies up to 1 kHz. Their measured 3 dB point is at 1.1 kHz for the one without the resistor and 6.5 kHz with the added resistor. In the following the coils are always used with this resistor not only to improve the frequency response also to produce more accurate magnetic fields, see Section 2.3.2.
The magnetic field of all coils is measured to test if all coils are wound correct and no damage to the cable was done during this process. The same method as in Sections 2.3.1 and 2.3.2 is used. The results are shown in Fig. 22. The three values of the magnetic field lie in this plot directly on top of each other, which is expected and show that these coils are similar. Only the x fit is displayed, because they are nearly the same and displaying all would lead to an unclear image. Also visible is that these coils produce the least magnetic field per current compared to all other tested coils, which was desired, see Section 2.2.

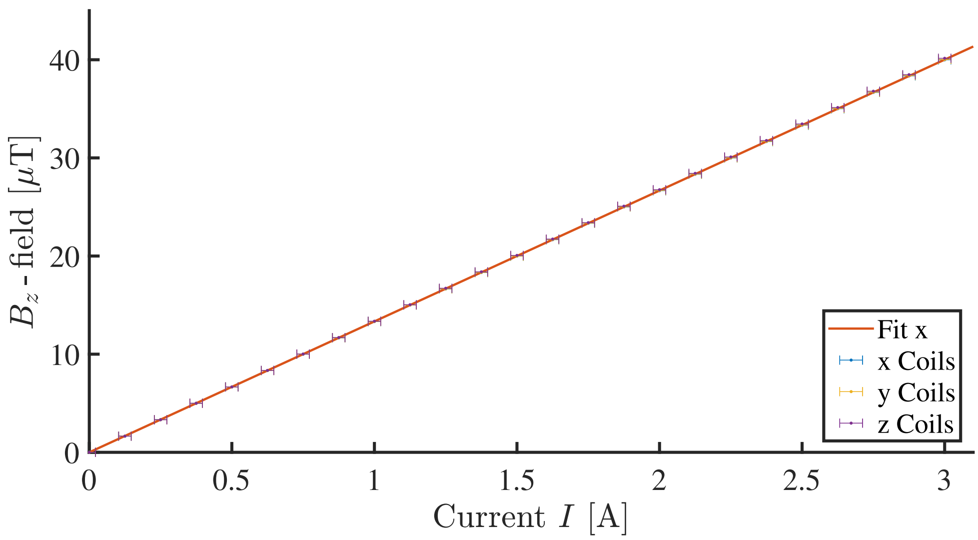

Figure 22: Magnetic field B_z generated by the three final coils in comparison to the field expected by the theory.

The fit function provides the fit parameter $\alpha = B/I$. It is shown in comparison with the theory in Tab. 11. The theory fits perfectly with the experimental data. To get an better estimate of the difference between the theory and the actual coils, the setup must be changed to a more precise current control to reduce the error bars.

Coil	$(B/I)_{\text{theo}}$		B/I	
	[μT/A]	[mG/A]	[μT/A]	[mG/A]
x	13.3	133	13.3(6)	133(6)
y	13.3	133	13.3(6)	133(6)
z	13.3	133	13.3(6)	133(6)

Table 11: Fitted values of for the magnetic field per current B/I, in comparison with the predicted values. The sated error is trough fitting a maximum/minimum linear curve through the error bars.

Another interesting measurement to take is the magnetic field measured at different spacial spots inside the coil system. For this measurement a constant current of 1 A is set to the EA-PS power supply. The senor was moved in steps of 2 cm, once in the direction of the axis of the coil pair, z direction, and once in a direction orthogonal to this axis, which means either x or y in this case. The magnetic field was only measured in the z direction, which is suitable enough to show that the calculated theory is also valid off center. The result is shown in Fig. 23. It is visible that the calculated Helmholtz configuration works as intended. Not only does the theory fits to the experimental data, there is also a large area at which the magnetic field is constant. The difference between measurement on and off axis is that the magnetic field drops faster at the edges. This drop starts to appear in both directions at around 8 cm to appear. According to the plot the magnetic field can be assumed to be homogeneous in z direction in an area of ± 6 cm. The error bars of the magnetic field, which comes as described in Section 2.3.1 mainly from the noise of the DAC, are supplemented by the error in spatial placement of the sensor it is assumed to be ± 2 mm because this time the sensor could not be mounted in a direct connection on to the optical table, instead has to be mounted on a metal rod where it is slid in to the right place by measuring the coordinate with a ruler.

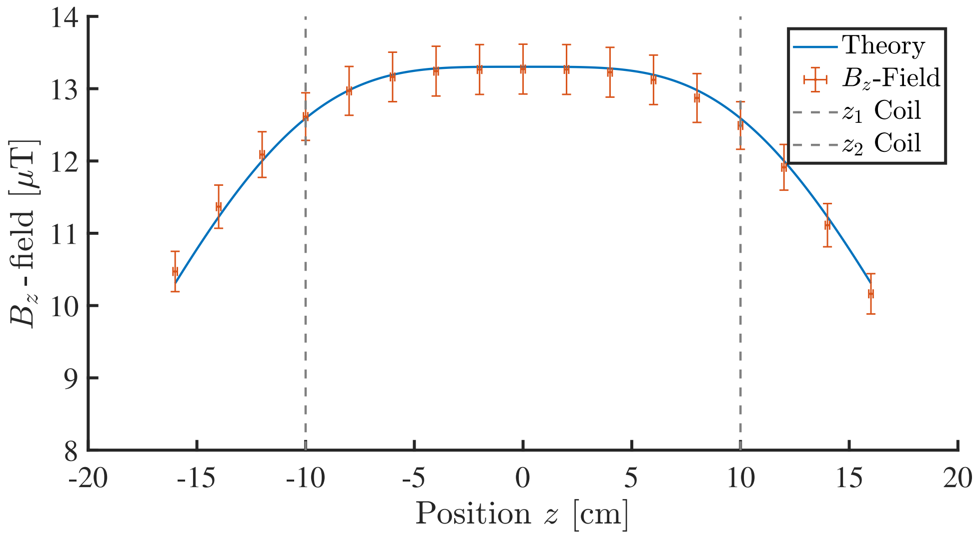

(a) Generated magnetic field B_z in dependence of the z direction.

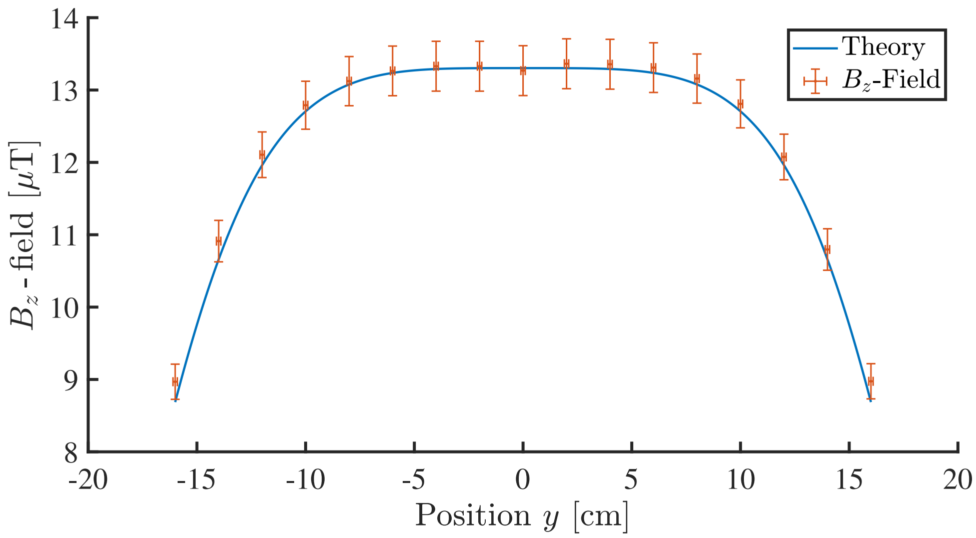

(b) Generated magnetic field B_z in dependence of the y direction.

Figure 23: Magnetic field B_z generated by the three final coils, with comparison to the field expected by the theory, under variation of the position of the magnetic field sensor in z and y direction.

3 Active Field Stabilisation

After successfully building coils which match the theory, the next important step is to control the induced magnetic field. The simplest way to do this was already done in Section 2.3. An input signal is sent to the system which is converted to a magnetic field. For better understanding see Fig. 24, but without the feedback line. This is good enough for measurements done in this chapter, because it is not necessary in these case to achieve an exactly given magnetic field. It is good enough to just exactly know the magnetic field at this time. An improvement is a good calibration of the factor or transfer function that connects the current with the **B** field, but method does still not compensates external influences like changing external magnetic fields that add to the generated field. To achieve this enhanced control it is necessary that the magnetic field is known and feedback to a control unit that it translates to an appropriate correcting value. In Fig. 24 a general concept of this principle is shown.

3.1 Theory of a PID Controller

A lot of different types of these controllers, all for different specific application, exist. For this case the first choice is to use a so called PID controller (PID). The name PID in an abbreviation which stands for

- P: proportional
- I: integral
- D: derivative.

A lot of textbooks [18–20] describe this common controller, how it works and how to benefit form it most is all kind of situations. To explain the PID controller a look at Fig. 24 is useful. As one input signal the controller needs a setpoint value. This is the value at which the desired variable should be. The second input that is needed is the actual value of the variable. As an output signal so called correcting variable is sent to the system, in this case to the power supply which controls the voltage/current in the coils.

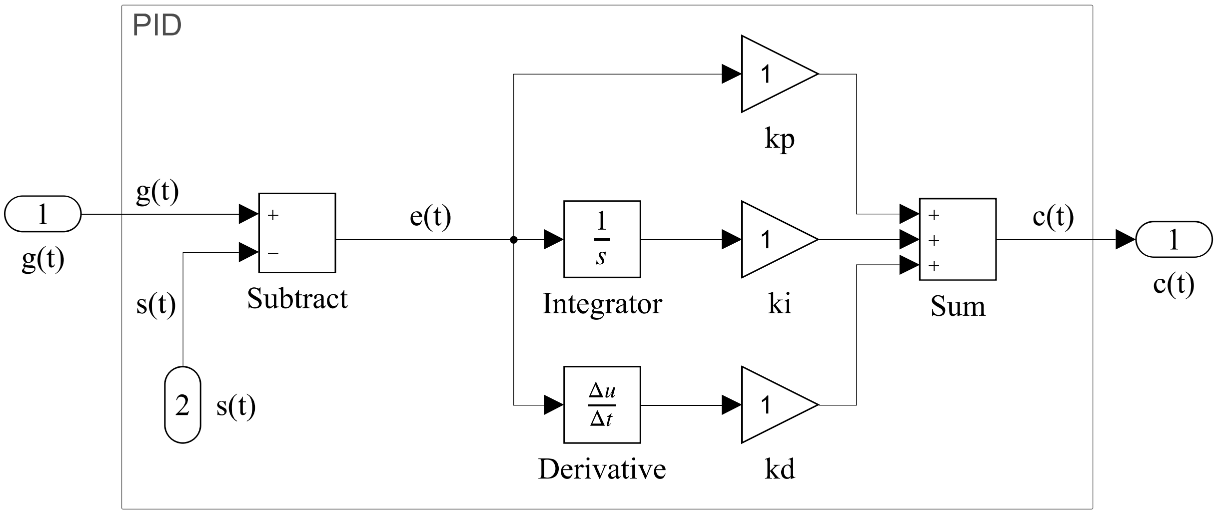

Figure 24: Theory of operation of a PID controller. First the difference between the signal to the desired set point is taken. This value is then computed by the individual PID part. Before a value leaves the controller the single values of each part are summed together.

The transfer function inside the PID controller is the part that differentiates this type of controller towards others. The first step of this controller takes the deviation between the actual signal $s(t)$ and the setpoint value $g(t)$ it is called error signal e.

$$e(t) = g(t) - s(t). \tag{3.1}$$

All the following steps are calculated with this quantity. The correcting value $c(t)$ is calculated in the following way

$$c(t) = k_P \cdot e(t) + k_i \cdot \int_0^t e(t')\, dt' + k_d \cdot \frac{\partial}{\partial t} e(t). \tag{3.2}$$

In this equation three constants are introduced.

- k_p is the constant for the proportional term. This is multiplied to the direct difference between the setpoint value and the actual one. This value determines the speed at with the signal first shoots towards the goal. A controller with only with this value would theoretically never reaches its goal in a perfect system, because it decreases linear with the error signal, which lead to the simple solution of the differential equation it describes, of an exponential decrease shifted up to the setpoint value.
- k_i is the factor multiplied to the term that solves this issue. It integrates the error over the time. This allows in theory the system to reaches its setpoint value. But a too large factor leads to an unstable system which is highly likely to overshoot the setpoint and diverges. The same problem occurs of course with k_p in a non ideal system, but this value is not as sensitive to this changes.
- k_d is multiplied with the derivative term. The purpose of this term is to detect large changes of the error value in time and tries to counteract to this. This is good

for decreasing the overshoot of the actual signal. The drawback of this term is, that the system has to have a high signal to noise ratio, because if the signal a lot of noise the deviation swaps form positive to negative sign nearly every measurement point. This is not always bad but if this change is to high it creates a artificial correction value, which again distorts the actual variable.

This controller can be easily modified to be a just a P- or a PI-, and so on, controller if the corresponding constants k are set to zero.

3.2 Components of the Digital PID

In previous chapter it was talked about measuring writing and computing data. Until now the only things that are mentioned are the chosen power supply and the used coils. An also important part is to choose the right secondary components.
The most important connection between the measurement and the evaluation is the magnetic field sensor. There are different types of sensors like a hall sensor, a superconducting quantum interference device (SQUID), NV centers in a diamond, or a flux gate sensor. The third type is used for this experiment. It consist of a magnetic susceptible core at which a coils is wrapped around this coil is driven with a periodic current [21]. With another coil the response of this field is measured. This signal can be the direct output signal or further processed by the sensor, for example rectified. The chosen sensor for this thesis was the FLC3-70 from Stefan Mayer Instruments [22]. It is right at the edge of what is possible right now with this technique. It has a good accuracy compared to the most hall sensors and a wide range and is easy to use compared to SQUIDs. It can sense magnetic fields in all three direction, that are in the range of $\pm 200\,\mu\mathrm{T}$. This is done up to a frequency of 1 kHz and with a noise smaller than $0.5\,\mathrm{nT}_{\mathrm{RMS}}$ or $3\,\mathrm{nT}_{\mathrm{PP}}$. The precision is at $\pm 1\% \pm 0.5\,\mu\mathrm{T}$, which is on the first glance not a good choice if the goal is to stabilise the magnetic field in the region of nT. Because it is one of the best sensors available for this purpose right now and the interest is in the stabilisation of the field, not in the actual value of the field the noise value is most important, because it describes the dynamic error of the system better. The only thing that has to kept in mind is that if a stabilisation is done around a specific value the actual stable field can deviate from this value of the amount given in the data sheet. The value of the field is presented by the sensor through voltages between V_{out} and the corresponding V_i. The color coding, which is not given in the data sheet, is shown in Tab. 12.

Wire color	Channel
Red	V_+
Black	V_-/GND
Green	V_{out}
Yellow	V_{x}
White	V_{y}
Blue	V_{z}

Table 12: Color coding of the Stefan Mayer Instruments FLC3-70 flux gate sensor.

This voltage has to be transmitted to a device that reads the voltage. This is done with a shielded, twisted cable to reduce the pickup of ambient stray electric fields in the signal. A BNC cable was not the best solution for this case, because it has three different output channels, which would lead to additional cables and rather complicate in and out coupling of the signal.
The voltage was then transmitted to an analog to digital converter (ADC) where it was converted to digital values. The choice of the ADC is the second important one to make. It has to be accurate enough to read the voltage to the desired limit, in an ideal case better than the sensor accuracy/noise. The sampling frequency, has to be high enough to represent the the signal, which means, according to the Nyquist theorem, twice the frequency. The chosen ADC is the AD4111 from Analog Devices. It comes mounted on an evaluation board, the EVAL-AD4111SDZ. It is a 24-bit analog to digital converter with eight voltage input channels. It can sample up to 31.25 kSPS with a single active channel, and 6.21 kSPS "per channel" if multiple channels are used. The noise of the channel is also very low, if the sampling frequency is reduced to 1.25 SPS than the noise is at ± 1 bit it goes up to about ± 75 bit if the sampling frequency is maxed out [23]. So the weak point is still the magnetic field sensor. The noise data was also tested and is shown in Fig. 25. The sampling frequency was chosen to be the same as used for the PID, 5.21 kSPS. The noise level of the measurement is higher than the values given in the data sheet. This is caused that the AD4111 is not tested under the same optimal conditions as for the data sheet test. It interacts with the evaluation board, the microcontroller and also the environment noise. The measured standard deviation is 93 μV. This is translates to a measured magnetic noise of $B_{\mathrm{rms}} = 3.3\,\mathrm{nT}$.

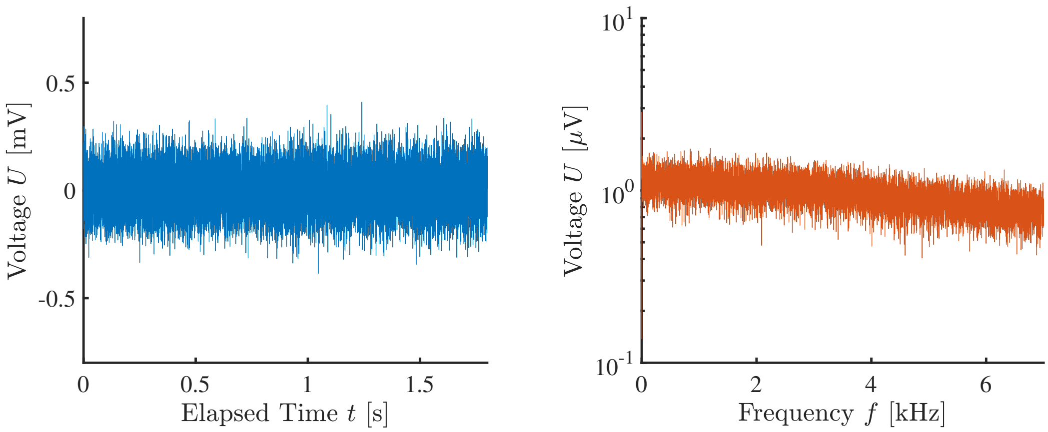

(a) Noise in time space. (b) Noise in frequency space.

Figure 25: Measured noise level of the AD4111, with shorted differential voltage input. Data is displayed in time and frequency space.

The digital value is transmitted via a SPI bus to a microcontroller (MCU). The one used is a Teensy 4.0. The advantage of this controller is that it has an easy program interface, the Arduino software and it is cheaper than an standard Arduino. Another advantage is that is has a very fast CPU with 600 MHz, that can be overclocked to 1 GHz, if really needed. It also has a built in floating point unit which performs 32-bit float operations at

similar speed as integer math. Double precision variables are handled at half the speed. By this values the microcontroller should also not be the bottle neck of the whole system. The output of the PID loop is a voltage. The device that converts the digital value to an analog one is called a digital to analog converter (DAC). The chosen one for this PID is the Texas Instruments DAC81408 [24], that also comes with a evaluation board the DAC81408EVM. It has a 16-bit output at several different voltage ranges. In this PID the smallest range from 0 V to 5 V is used, because then the DAC has the lowest voltage per bit ratio. With the same argument the range ±2.5 V could have been used, but it makes in this case no difference, but the slew rate in the first case is four times lower at 1 V/μs. The sample speed is limited by the settling time $t = 12\,\mu$s and the bus speed, which represents the time that it takes to upload the data to the DAC. Converting the settling time to a frequency, the result is $f = 83.3\,$kHz way above the frequency limit of the magnetic field sensor of 1 kHz.
But there are also drawbacks of this components, which can not be foreseen in the data sheet, or have a vague presentation in it. The noise level increases a lot if the SPI clock is active. This is of course necessary to transmit new data to it or read incoming data from the ADC. That this noise is coupled to clock cycle can be seen in Fig. 26. At first the clock signal is of and then a new data set is transmitted and the output voltage shows the square modulation. This can be reduced with decoupling the digital ground and the analog ground, not having the Teensy and the ADC share the same ground, for example with multiple optocouplers. The impact of this problem decreases with increasing clock frequency. The chosen clock frequency for the SPI communication is 20 MHz, so this signal cannot be measured with the ADC, so it would not add a lot of noise to the signal read. The power supplies are also not capable of supplying this frequency, compare with the 3 dB frequency $f = 140\,$kHz of the OPA548, Fig. 10. With connected coils it decreases even further, Fig. 21.

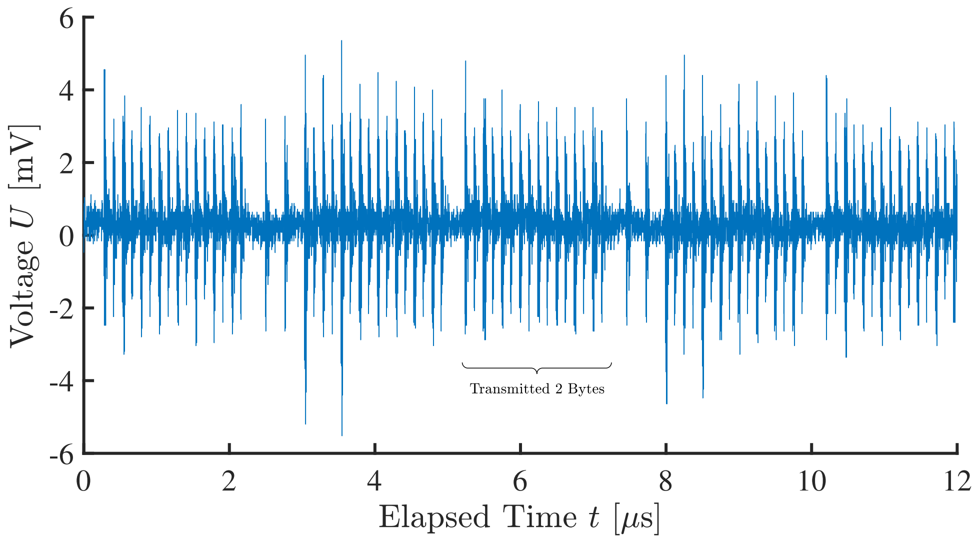

Figure 26: Measured noise of the output voltage of the DAC81408EVM board. The important thing to see is the coupling to the SPI-clock signal, which is used to communicate.

The ADC evaluation board does not has this noise issue, one reason is because it has an already inbuilt decoupling component on the board and it can sample only to 31.25 kHz. The problem with this board is the sampling rate. The stated 31.25 kSPS for a single active channel and the 6.21 kSPS "per channel" sound good. The problem with the single active channel is that it has a settling time of 161 μs, which corresponds to the 6.21 kSPS. The vagueness becomes through the fact that this value is always stated after the multi channel sampling rate and corresponds to that. In reality the ADC buffers five measurement and the first data is available if the 6th measurement is taken. This means it has the stated sampling rate but the delay is five times larger than the expected one of around the time between two measurements. This decreases the capability of the PID to counteract higher frequencies, because it takes at least twice the time of 161 μs to let the PID to the result that it has written. This problem becomes visible in Fig. 27.

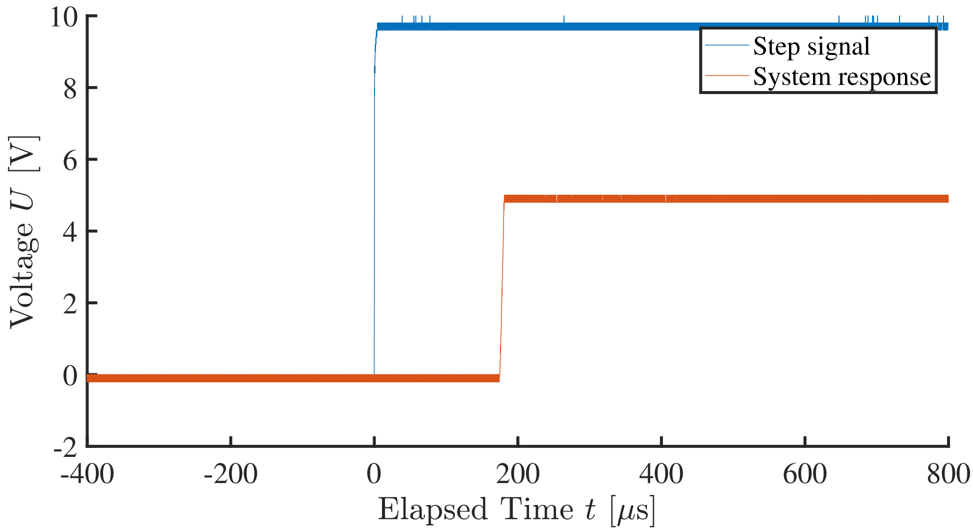

Figure 27: Mirroring of a square shape signal with the active PID system. With this the time delay between a measurement and a reaction of the PID system can be determined.

In this plot a square signal is supplied to the ADC, the microcontroller performs its normal PID loop, but reacts to the square signal by mirroring these signal at one output port of the DAC. With this the response time of the whole PID system is visible, it is around $t = 178(4)\,\mu$s. To specify the time of each component, they can be exclude from this test and the measured time difference is the time that this specific component consumes. In Tab. 13 the time for each of the three components is recorded. This table shows that the slowest component is the ADC and should be the first thing that is exchanged to achieve a faster PID. The MCU takes only a very small amount of time to compute the the PID correction values and is due to this should be considered as suitable enough for this PID system. One thing that has to be kept in mind, by doing this measurement additional time is added to the whole loop, due to very few extra lines of code, the mirroring of the step function. Also with excluding one of the other two components that are not the MCU, the in and output port of the MCU itself also have a time delay, but this one is considered faster.

Component	t [μs]
ADC time to measure	164(3) μs
PID computation time	4(2) μs
DAC time to output	10(3) μs

Table 13: Time response of each component of the PID system.

The next problem that comes with the ADC is the multi channel property. In the data sheet it is stated as "Channel scan data rate of 6.21 kSPS per channel" [23]. If multiple channels are activated in the PID, the sample rate drops to this value. The time between two data points of different channels has a time of 161 μs which corresponds to this 6.21 kSPS. No matter how much channels n are active this number stays constant. It means the real frequency per channel is $6.21/n$ kSPS. This also reduced the PID speed, if used in all three directions by a third.

3.3 Tuning Method

A PID controller needs good values for the constants k_p, k_i and k_d, Section 3.1, to work in the intended way. Finding these values can be sometimes a very challenging task to fulfill, not only because a PID takes three variables, which heavily influence each other. To find the right values the work of Ziegler and Nichols [25] was used in this theses. The method makes use of a calibration step in which the necessary values are determined to calculate close to optimal constants.
This calibration can be done in two different ways. The first method makes use of a sudden jump of the measured variable. The resulting shape of the slope gives, after some processing, the desired constants.
The other method and chosen one is dynamic measure. In this case all constants are set to zero, after this the proportional constant is increased until a value is reached at which the signal is is oscillating with a constant amplitude. The value of k_p at this point is called the ultimate gain k_u, the oscillation frequency is $f_u = 1/T_u$. In the paper of Ziegler and Nichols, all values for k in the three most common configurations are given. The definition of their constants a_j is different compared to the ones used in Eqn. (3.2). The conversion is given by

$$k_p = k_p; \qquad k_i = k_p/T_i; \qquad k_d = k_p\,T_d, \tag{3.3}$$

where

$$T_j = \frac{1}{a_j}\,T_u. \tag{3.4}$$

The transformed constants for all three combinations are listed in Tab. 14. This constants are used for all measurements in this thesis, a bit of tweaking is possible to find a slightly better result, but would require an unreasonable amount of time compared to the prototype character of the setup.

Type	k_p	k_i	k_d
P	$0.5\,k_u$	—	—
PI	$0.45\,k_u$	$0.54\,k_u/T_u$	—
PID	$0.6\,k_u$	$1.2\,k_u/T_u$	$0.075\,k_u\,T_u$

Table 14: Tuning values for the constants k for different controllers types, according to the Ziegler-Nichols method. The ultimate gain k_u describes the value of k_p at which the measurement oscillates. The oscillation period is give by T_u.[25]

The actual tuning method has to be a little bit modified. In the paper the oscillation started from a infinitesimal deviation from the setpoint where the signal it self seems to be rather constant. This is the complete opposite to the situation present in this setup. The signal of the magnetic field already oscillates at a non-negligible amount, compared to the amplitude at ultimate gain. This makes it impossible to determine the exact point at which the oscillation is driven by the PID and not by the external field, because there is always a non-stable oscillation which is combined of these both. A solution to this problem is to increase the amplitude of the driven oscillation. This can be done if the setpoint is not at the same value where the field is, at the time when the PID is initialised. This leads to a large correction $c(0)$, that leads directly to a larger overshoot at the point where the setpoint is reached. The driven oscillation amplitude sets itself apart and k_u, T_u can be determined.

3.4 Experimental Data and Results

This section shows the experimental data that is collected under consideration of the thoughts and theory discussed in Sections 3.1 and 3.3. All measurements are done with the same setup, the part that is changing is the coil.

3.4.1 Old Coils

First the experimental setup is discussed. The setup that is used to stabilise the magnetic field is similar to the one used to measure the magnetic field per current, Fig. 16. The difference to that setup is the code that runs on the microcontroller and the carefully chosen surrounding electrical components of the coils. Due to that the general background noise can be reduced. The sample rate of the analog to digital converter was from 31.25 kSPS reduced to 5.21 kSPS to avoid issues that occur, because the magnetic field sensor is over sampled. But value is also higher than two times the frequency of the fluxgate sensor of 1 kHz to to preserve the general shape of the signal. In this chapter not all three axes of the coil system are used. Only the z coils are examined, because the sensor alignment was the most precise in this case and these coils are replaced by the final ones anyway. The measurement should only be a comparison to a non-optimal coil.
The first thing that has to be done is to find proper values for the PID controller. This is done with the Ziegler-Nichols method described in Section 3.3. A magnetic field is generated and at a specific time during the recording the PID is turned on to jump towards a

slightly different value. For this case only k_p is used, so its technically only a P controller. This constant is now increased to a level were the magnetic field oscillates at a constant amplitude. In all cases this was not possible to achieve with a accuracy of 2 digits of k_p. That means that means that there exist two values right next to each other, at the higher one the magnetic field diverges over time and at the lower one the magnetic field converges. The lower one is used to calculate the actual values given by the Ziegler-Nichols method. These computation values are shown in Tab. 14. The required oscillation period time is directly read out of the data. Therefor the time of 10 periods is measured and divided by ten to achieve a good average. The actual values k_j for each controller type are given in Tab. 15. These constants are dimensionless, respectively multiplied/divided by a time. They take into account all conversions between the single components, for example the voltage output of the sensor compared to the magnetic field of 35 μT/mV.

Type	k_p $[10^{-4}]$	k_i $[10^{-2}\,1/\text{s}]$	k_d $[10^{-7}]$s
P	2.50	—	—
PI	2.25	4.05	—
PID	3.00	9.00	2.50

Table 15: Tuning values for the PID used with the old coils. They are determined by the Ziegler-Nichols method with an ultimate gain value of $k_u = 5.0 \times 10^{-4}$ and a oscillation period of $T_u = 6.7\,\text{ms}$.

In Fig. 28 the measurement to determine the value of the ultimate gain k_u and the oscillation time T_u is show. It also compared to the step response of the final PID with all three constants used, to show that the oscillation actually has a stable behavior around the setpoint. The determined $k_u = 5.0 \times 10^{-4}$ and the periodic time $T_u = 6.7\,\text{ms}$.

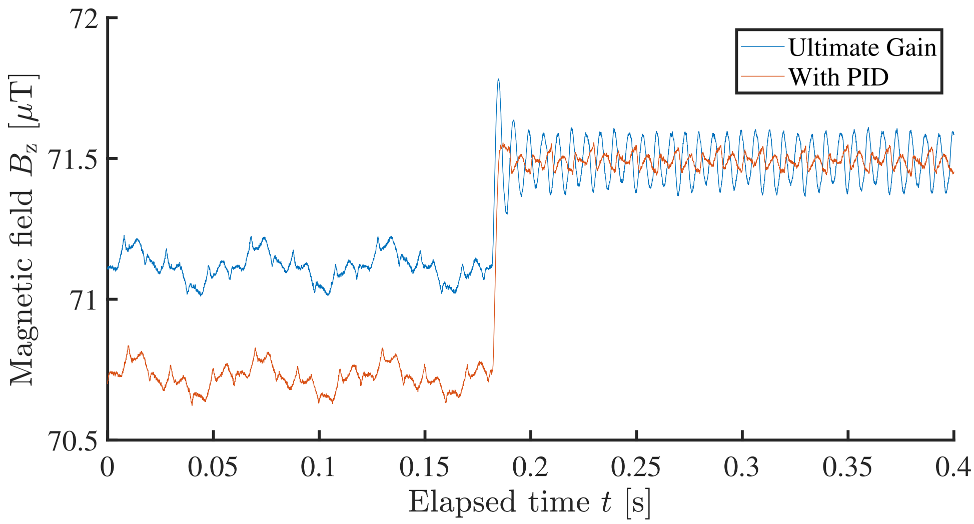

Figure 28: PID step response at ultimate gain. Tuning on the PID controller leads to a sudden increase of the magnetic field and a stable oscillation at ultimate gain.

This figure shows a nice stable oscillation after the first big amplitude, which is caused by the step. It is also visible that the PID controlled course has a smaller oscillation than the signal without a controller. This result is better visible in the frequency domain. For this the code is changed, so the PID controller is turned on around one second before the actual measurement starts. With this the initial oscillation, which is caused by the activation of the PID is cut off as well as the step itself. From this the fast Fourier transformation (FFT) is computed, but the average magnetic field of the signal is subtracted before it to remove the zero frequency value. This procedure was done 10 times to be able to calculate an average of the FFT, which leads to a way smoother result. The average of the single-sided amplitude spectrum is shown in Fig. 29. In this plot all three common controller configurations are shown in comparison to the background noise.

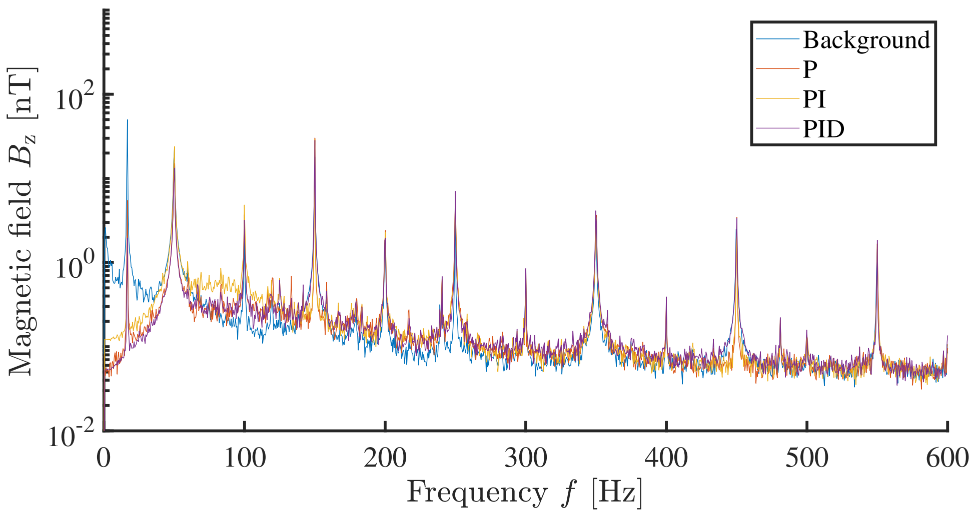

Figure 29: Measured magnetic field in frequency space with different controller types, P, PI and PID. The results are plotted in comparison to the magnetic background noise.

The most common and expected peak is the peak at 50 Hz. This one is generated by the normal AC grid, which supply every component with a mains plug. Higher harmonics, like 100 Hz, 150 Hz... of this signal are also visible and build up the main peaks in the FFT. One dominant peak an 16.67 Hz can not be referred to this power grid. It is caused by the train, which runs underneath the university building. This peak deviates also a lot in height, which is caused by passing trains and makes it necessary to average over a longer time. The total measurement process takes around 5 minutes, which should be long enough to record at least one passing train. With this time the deviation caused by theses trains is minimized under a reasonable amount of measurement time and averages. The next step is to analyse the FFT curves of the different controllers. At really low frequencies the PID works good. It decreases the 16.67 Hz peak about one order of magnitude. This capability vanishes quickly and is at the 50 Hz not there anymore. At this peak the difference between the three controller types is visible. Before this all controllers perform quite similar, where the PI controller was a little bit worse. The P and the PID are in this case at the same level. The PI is a little bit higher than these two and has even an overshoot of the actual noise signal between 50 Hz-150 Hz. This is expected because the PI controller is designed to have a little bit of overshoot of the setpoint in the time domain, which leads to a short oscillation. The additional derivative term is meant to reduce this, which is also visible. To conclude this measurement, these coils are effective at frequencies below 50 Hz. They reduce the standard deviation of the magnetic field with a PID controller from 49 nT background deviation to 28 nT ($\sim 45\,\%$ decrease). The peak to peak value decreases from initial 278 nT to 152 nT with the PID ($\sim 46\,\%$ decrease).

3.4.2 Cylindrical Coils

This leads to the next coils, which are the first specific ones that are designed for this purpose. They have a better frequency response than the old coils, see Section 2.3.2, which should directly translates to a higher effective stabilisation frequency. Before this measurement is done the PID has to be tuned first. This is done the same way as for the old coil. The Fig. 30 shows the step performance at ultimate gain. This time the PID response was not shown to keep a clear visual of the oscillation at ultimate gain. Due to the fast oscillation the additional data of the tuned PID would lead to dense lines which could not be distinguished from each other. The oscillation is not constant is this case. As described in Section 3.4.1 the shown step response is at the highest possible k_u without causing a divergence. The oscillation decreases until a sharp peak of the background field occurs. These peaks can be seen in the section without the PID and occur with a frequency of 50 Hz.

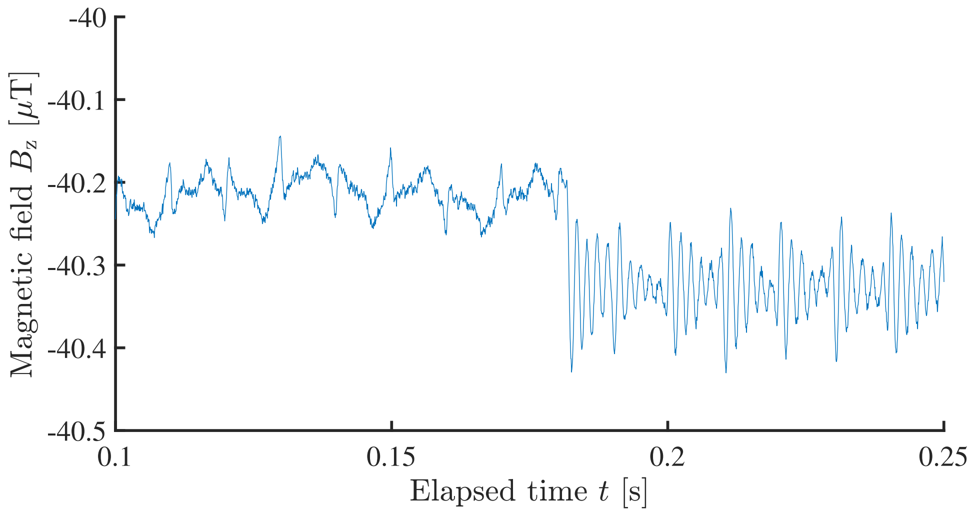

Figure 30: Magnetic field inside a cylindrical coil before and after a PID controller is activated. The oscillation are induced to a mixture of the ultimate gain oscillations and the background noise.

Out of this plot a ultimate gain of $k_u = 3.0 \times 10^{-3}$ and a oscillation period $T_u = 1.8\,\text{ms}$ are determined. This leads to the PID constants given in Tab. 16.

Type	k_p $[10^{-3}]$	k_i $[10^{-1}\,1/\mathrm{s}]$	k_d $[10^{-7}]\mathrm{s}$
P	1.50	—	—
PI	1.35	0.89	—
PID	1.80	1.98	4.09

Table 16: Tuning values for the PID used with the cylindrical coil. They are determined by the Ziegler-Nichols method with an ultimate gain value of $k_u = 3.0 \times 10^{-3}$ and a oscillation period of $T_u = 1.8\,\mathrm{ms}$.

The FFT of the different controllers is also done the same way as in Section 3.4.1 and is shown in Fig. 31. This time the curves with the controller catches up with the background noise at around 200 Hz, which is 4 times better than with the other coils. Another difference is that the P and the PI controller have with this coil the similar values. Only the derivative term, PID, reduces the magnetic field at low frequencies even further. At the 16.67 Hz peak the amplitude is reduced by more than two orders of magnitude and at 50 Hz still more than one order of magnitude. The fact that the derivative is necessary could be an indicator that the coils is not the limiting factor. The controller reaches its limit and needs to predict the future with derivative term to improve its result. At higher frequencies the controller increases the magnetic field oscillation, because of the already mentioned induced overshoot.
It was possible to stabilise the magnetic field from a value of 54 nT background standard deviation to 24 nT ($\sim 46\%$ decrease). The peak to peak value went down from 285 nT to 173 nT with active PID ($\sim 61\%$ decrease).

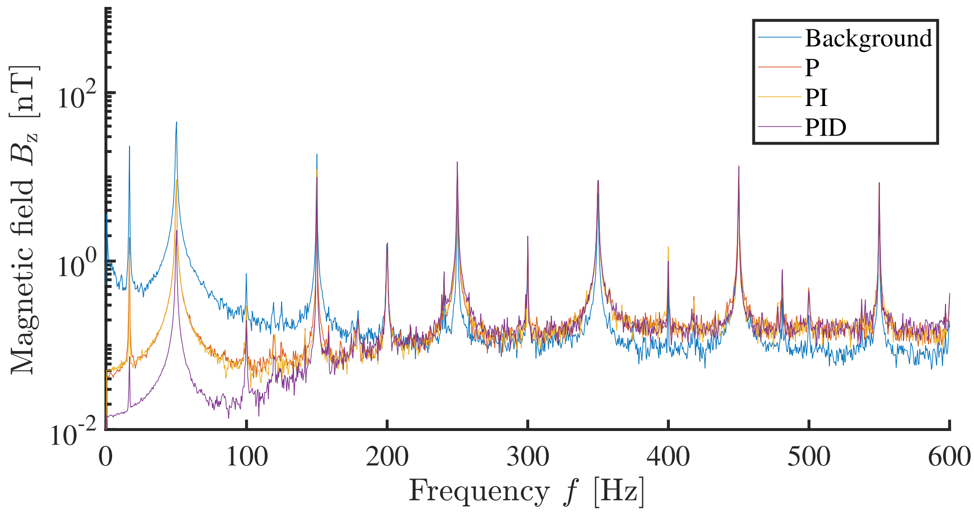

Figure 31: Fast Fourier transformation of the magnetic field with different controller types, P, PI and PID. The results are plotted in comparison to the magnetic background noise.

3.4.3 Triple Helmholtz Coils

The final coil system consist of three identical coils, but only the z direction is reviewed in this part. All measurements can be directly transferred to the other two. Apart from this is that tuning is the same compared to Sections 3.4.1 and 3.4.2.

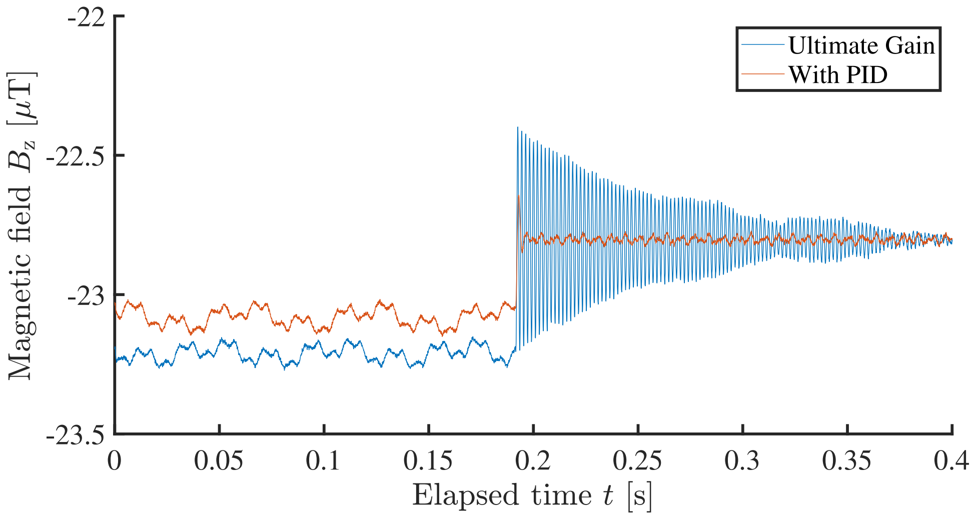

Figure 32: Magnetic field inside the final coils, before and after turning of the PID controller. The controller at ultimate gain is displayed along side with the tuned PID controller.

The step operation, Fig. 32 results again in an oscillation which decreases slowly. The next higher value of k_u with in an accuracy of two digits would lead an unstable oscillation. This time no 50 Hz pattern is visible in the oscillation after the controller has started, there are also the sharp peaks missing in the background field. The determined value for the ultimate gain was $k_u = 3.1 \times 10^{-2}$ and for the oscillation period $T_u = 1.9\,\mathrm{ms}$, which leads with the Ziegler-Nichols method to the results in Tab. 17.

Type	k_p $[10^{-2}]$	k_i $[10^1]$ 1/s]	k_d $[10^{-6}]$s
P	1.55	—	—
PI	1.40	0.90	—
PID	1.86	1.99	4.35

Table 17: Tuning values for the PID used with the final coils in one direction. They are determined by the Ziegler-Nichols method with an ultimate gain value of $k_u = 3.1 \times 10^{-2}$ and a oscillation period of $T_u = 1.9\,\mathrm{ms}$.

Using this constants the magnetic field modulated by the corresponding controller is given in Fig. 33. The performance similar to the one with the small coils. The P and PID controller intersect the background field fluctuations at 200 Hz. The PID controller is still the best option of all three types, but even this one is at higher frequencies above the background noise. It is capable of reducing the amplitude at 16.67 Hz about 2 orders of magnitude and at 50 Hz of 1 order of magnitude. Due to the overshoot of all controllers, especially the PID, further tuning can be done. This would deviate from the Ziegler-Nichols values a bit. The fact that the amplitude of the controlled signal is higher than the background noise at high frequencies, would be decreased if a combination is chosen in where no overshoot in the step response is visible. This means that the system is critical or even over damped and no artificial induced oscillations occur.

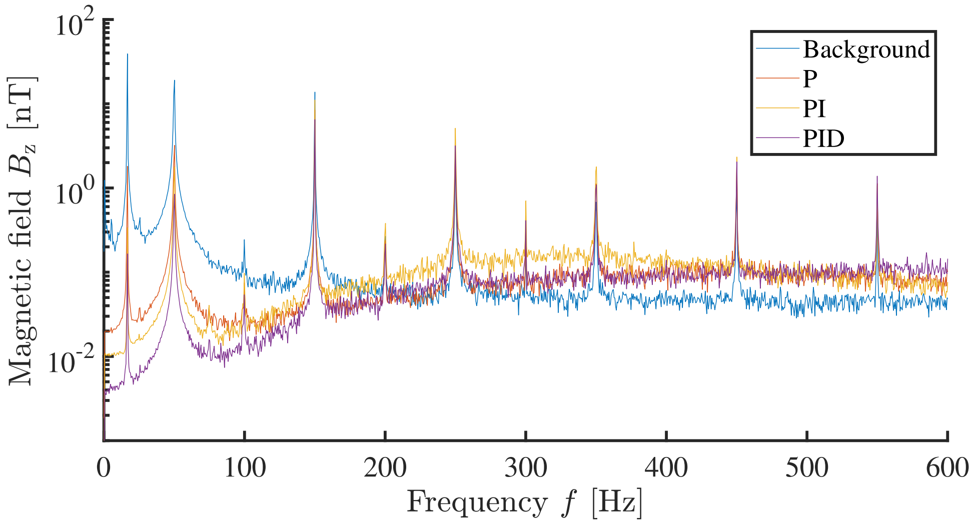

Figure 33: Measured magnetic field inside the final coils in one direction with different controller types, P, PI and PID. The result is displayed in frequency space in comparison to the magnetic background noise.

The final coils achieve a stabilisation of the magnetic field to a value from a background standard deviation of 39 nT to 8 nT with active stabilisation ($\sim$ 80% decrease). The peak to peak value decreases from 213 nT to 60 nT ($\sim$ 72% decrease).

4 Three-Axis Field Stabilisation

The results taken in Section 3.4.3 are the stabilisation in only the z direction. In most cases the interest is to stabilise the magnetic field in all three spatial directions. This is also true for this experiment.

4.1 Adjustments to the Controller

Before a PID controller is hooked up to each of the three coils some thoughts have to be made to get the best result. If the sensor is perfectly centred and aligned to the coordinate system of the coils, they would only produce a **B** field that is been measured by a separate channel of the sensor for each coil. In this case it is possible to use three independent PIDs or even take a common analog PID controller and the result would be sufficient. In reality this is not the case, because in the alignment of the sensor and the orientation of the coils is not on point. To compensate this issue a mathematical conversion is needed that couples the three PIDs. In Fig. 34 the principle of the improved controller is shown.

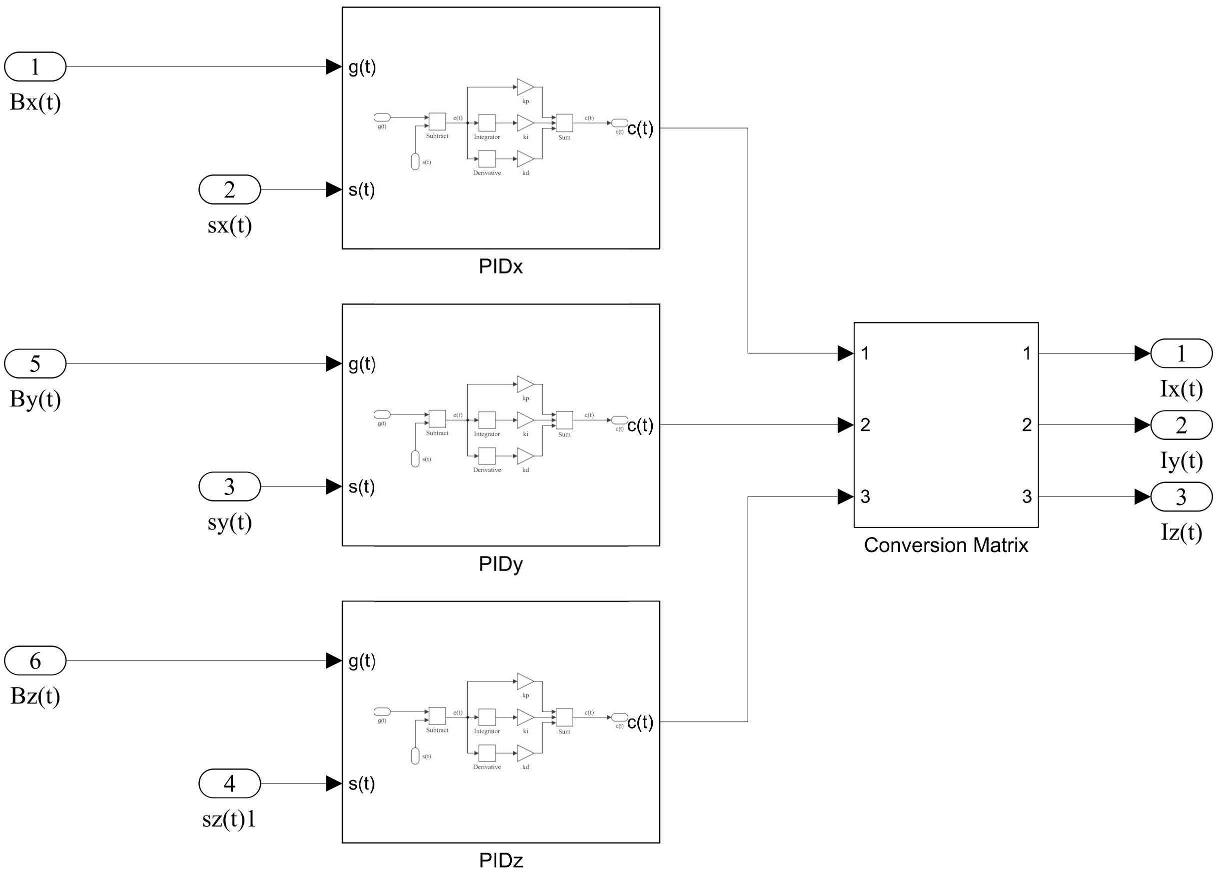

Figure 34: Schematic of a three-dimensional PID controller with coupled single PIDs for independent directions. The conversion matrix enables precise control of individual directions of the magnetic field picked up by the sensor.

The first thing that has to be determined is the magnetic field that is produced by every single coil itself. It is done by only sweeping a current through one coil at the time. This generated field is measured with the sensor in all three direction. Fitting a linear function to every data set for all three coils gives the magnetic field B_i increase per current I_j of the corresponding coil. These constants are named as followed

$$B_i = a_i^{\ j}\, I_j. \tag{4.1}$$

The indexes $i, j \in \{1, 2, 3\}$ resemble the measured/modulated spatial direction. It is visible that $a_i^{\ j}$ resembles a rank two tensor, also called matrix. The controller wants to control the magnetic field by writing a current, that means the Eqn. (4.1) has to be flipped and $a_i^{\ j}$ has to be inverted to

$$I_j = a^i_{\ j}\, B_i. \tag{4.2}$$

With this it is possible for the controller to determine the right current to produce an additional magnetic field. The matrix $a^i_{\ j}$ takes care of the right amount of current in each coil to produce the desired field.
In the experiment measured matrix and its inverted counterpart is given by

$$a = \begin{pmatrix} 7.8565 & -0.0438 & 0.1577 \\ 0.0313 & 8.1584 & 0.0939 \\ 0.0980 & -0.0003 & 8.0937 \end{pmatrix} \Leftrightarrow a^{-1} = \begin{pmatrix} 0.1273 & 0.0007 & -0.0025 \\ -0.0005 & 0.1226 & -0.0014 \\ -0.0015 & -0.0000 & 0.1236 \end{pmatrix}. \tag{4.3}$$

From the matrix $a_i^{\ j}$ the orientation and the goodness the alignment can be obtained. From this result it is again visible that the alignment was not bad. The matrix can not be completely diagonalized, because of the slight rotation of the coils in respect to each other. This method gives a result about the sensor alignment to the coils and about the coil alignment in respect to each other.
With this formalism it is possible to realise a stabilisation of magnetic field with nearly every sensor position and alignment. It is even possible to stabilise the magnetic field not at the point where the sensor sits, but for example at a science cell, if the magnetic field is not isotropic. Only an addition conversion matrix that connects the sensor readings with the $\mathbf{B}$ field at the desired spot is necessary. This emphasizes the need of a digital PID, because that is not as simple with the standard, non coupled analog PIDs.

4.2 Experimental Results and Data

The experimental setup in comparison to the one described in Section 4.1 has not change and the measurements were taken immediately after the determination of the conversion matrix $\mathbf{a}$. This means that this matrix was used and valid for each case. As with the single directional PID the three-directional controller has to be tuned. In this case the sampling frequency is increased to the maximum possible of 6.21 kSPS between each measurement, which leads to an effective sample rate of 2.07 kSPS per real channel. Apart from that the tuning is done exactly the same way as before with one active direction at the time. Due to the precisely similar design of the coils and the use of the same type of power supply the values at ultimate gain should be the same. The experiment proves this statement, that is why in Fig. 35 only the oscillation of the field in z direction is shown, if the z directional controller is activated. The values are $k_u = 4.2 \times 10^{-1}$ and for the oscillation period $T_u = 2.6\,\mathrm{ms}$.

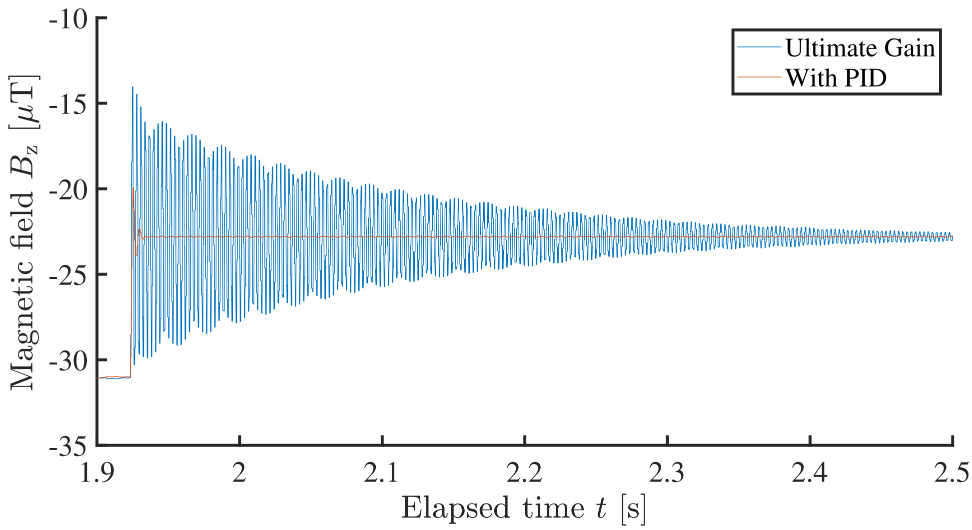

Figure 35: Response of the magnetic field in z direction B_z of the final z coil before and after turning on a PID controller at ultimate gain. In comparison to that the step response of a tuned controller is displayed.

These to values lead with the Ziegler-Nichols method to the controller values given in Tab. 14.

Type	k_p [10^{-1}]	k_i [10[2] 1/s]	k_d [10^{-5}]s
P	2.10	—	—
PI	1.89	0.88	—
PID	2.52	1.96	8.12

Table 18: Corresponding PID values that are obtained from the Ziegler-Nichols tuning method with an ultimate gain of $k_u = 4.2 \times 10^{-1}$ and for the oscillation period $T_u = 2.6\,\mathrm{ms}$. The values are for all three coil pairs the same.

If these values are put into the code the fast Fourier transform of the stabilised signal can be recorded and computed. The norm of the magnetic field is plotted in Fig. 36, to see the capability of reducing the total amplitude of the magnetic field in one plot.

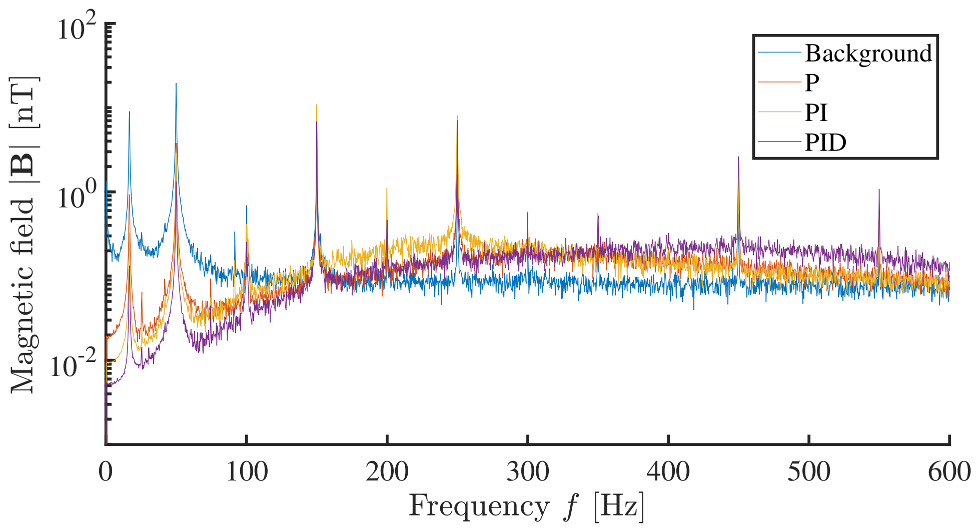

Figure 36: Fast Fourier transformation of the norm magnetic field inside the final coils with stabilisation in all three directions.

This plot shows similar behavior as the FFT's in Section 2.3. In this case the P is the worst at low frequencies, but it is close to the values of the PI controller. The maximum effective frequency is in this case decreased to 150 Hz. They both reduce the amplitude at 16.67 Hz about one order of magnitude and perform still quite good at 50 Hz. The PID controller is the best of all. It decreases the amplitude at 16.67 Hz close to two order of magnitude and at 50 Hz still better than one order of magnitude. All four curves intersect each other at 150 Hz. This value is not as good as the value for the stabilisation in one direction only. This is expected due to the fact that the ADC has to recorded three times more data, which leads regardless of the increase of the sampling frequency from 5.20 kSPS to 6.21 kSPS, to a total decrease of this sample rate to 6.21 kSPS/3 = 2.07 kSPS. This corresponds also with a way longer time of 1 ms, that the controller has to wait to evaluate its written change to one direction.

The fact that the PI controller has a higher amplitude at medium frequencies than the background field is already discussed in Section 3.4.1 and is caused by the intended overshoot of the setpoint. Dependent of the maximum frequency that is relevant for the experiment, it could be necessary to tune the PID values so that there is no overshoot of the setpoint. This means the oscillation is critically or even over damped and it would decrease the amplitude at higher frequencies to the level of the background field. The drawback of this, is that the performance at lower frequencies is not as good anymore.

This PID controller achieve a maximum stabilisation of the magnetic field in all three spatial directions form a background standard deviation of 26 nT to 11 nT ($\sim$ 57 % decrease). This result is only 3 nT higher than the result obtained with one active stabilization axis. The peak to peak value was initially 134 nT and is decreased to 77 nT ($\sim$ 43 % decrease). The second interesting thing to look at is the the orientation and its deviation of the magnetic field. This can be shown in a good way if $\mathbf{B}$ is transformed to spherical coordinates. The absolute value $B_r = |\mathbf{B}|$ was already discussed. The angular parts B_ϕ, B_θ are the interesting ones in this case. For the background noise this transformation is trivial, they are shown in Fig. 38a. For the value of the stabilised field it gets a little bit complicated. It is possible to compute these angles exactly the same way, the result is shown in Fig. 38b. But the direct comparison could be deceiving. The reason for this is shown in Fig. 37.

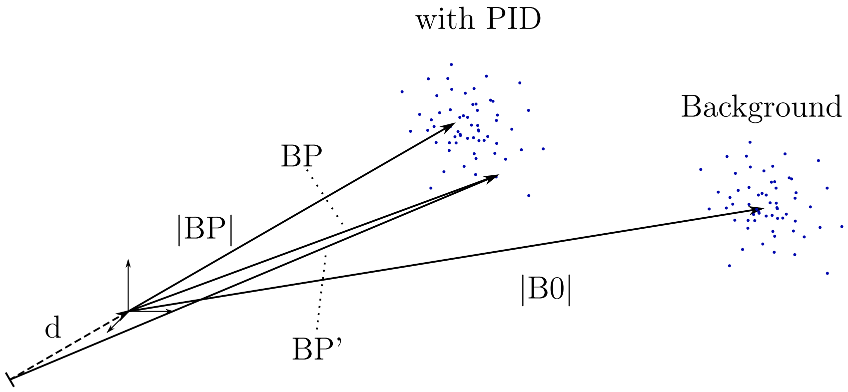

Figure 37: Schematic of the normalization of the measuerd $\mathbf{B}_{\mathrm{PID}}$ (BP) to $\mathbf{B}'_{\mathrm{PID}}$ (BP'). The vector of mean magnetic field with PID $|\mathbf{B}_{\mathrm{PID}}|$ (|BP|) is elongated with $\mathbf{d}$ (d) to the length of the mean of the background magnetic field $|\bar{\mathbf{B}}_0|$. This creates comparable angel distributions for both data sets.

If the stabilised field has a higher absolute value the angle components would deviate less even if the absolute magnetic field has the same deviation in each spatial direction. This occurs due to the non linear transformation into spherical coordinates. To get a better impression of the capability of the PID controller the measured vectors $\mathbf{B}_{\mathrm{PID}}$ have to be normalized to the length of the medium absolute field without any stabilisation. This means measuring the field with the PID from an artificial zero point, so the mean of the normalized vectors $\mathbf{B}'_{\mathrm{PID}}$ has the same norm as the one of the background $\bar{\mathbf{B}}_0$. This leads to the conversion formula

$$\mathbf{B}'_{\mathrm{PID}} = \mathbf{B}_{\mathrm{PID}} + \underbrace{\left(\frac{|\bar{\mathbf{B}}_0|}{|\bar{\mathbf{B}}_{\mathrm{PID}}|} - 1 \right) \bar{\mathbf{B}}_{\mathrm{PID}}}_{\mathbf{d}} . \tag{4.4}$$

With this the last picture, Fig. 38c, can be computed.

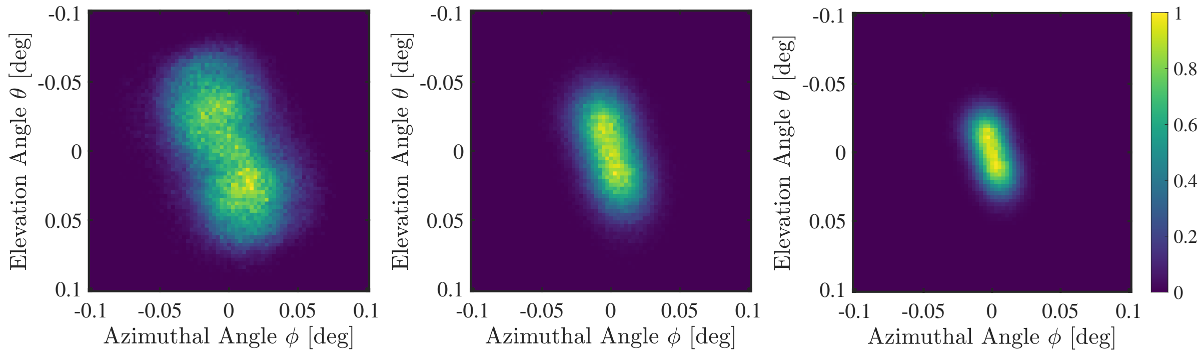

(a) Background. (b) With PID. (c) With PID (normalized).

Figure 38: Angle distribution of the magnetic field vector of the background noise (a) and the stabilised field (b). In addition to these, a map in which the stabilised magnetic field vector is normalized to the amplitude of the background noise is displayed, to show the angle distribution at similar amplitudes (c).

This shows the distribution of the angle of the magnetic field. In every sub picture the mean angle is subtracted from the measurements to center the complete point cloud. In Fig. 38a the angle deviation of the background is shown. Important for the comparison is the norm of the mean field, it is $|\bar{\mathbf{B}}_0| = 52.4\,\mu$T. The shape of the cloud has the appearance of a peanut, with two larger sides and a smaller middle part. This figure has an defined axis. If the deviation is completely homogeneous in every spatial direction the shape would be an perfect circle. This would also be the case if this deviation is only caused by noise, which is equal on every channel. The most likely explanation of this shape is an antenna, for example an simple straight wire, which produces an alternating magnetic field in a specific spatial direction. The most dominant fluctuations are caused by the 50 Hz power grid, which all around the experiment and the 16.67 Hz power grid of the train. Especially this one can be seen as a wire, because the rails are on the scale of the experiment far away. This leads to the appropriate approximation of single wire antenna.

The two pictures Figs. 38b and 38c show the deviation with stabilisation turned on. The middle one Fig. 38b is not normalized and shows the actual value. For better comparison to the background picture the Fig. 38c is normalized like Eqn. (4.4), to the amplitude of the background field. It is a little bit smaller than the not normalized one, because the PID generates an absolute field of $|\bar{\mathbf{B}}_{\mathrm{PID}}| = 36.0\,\mu$T which is smaller than the background noise. The shape also changes from a bimodal mode, with two dense edges, to single mode distribution, that has a uniform distribution along its axis. The important thing to see is that the PID not only reduces the fluctuation of the norm of the magnetic field, it also stabilises the field directions.

A final remark to this method, the fluctuation of the angle is very small. The background field has a maximal deviation of $\pm\,0.08\,^{\circ}$ and the stabilised field of $\pm\,0.04\,^{\circ}$, or $\pm\,0.03\,^{\circ}$.

4.3 Rotation of the Sensor off Axis

The last thing that is interesting is impact of the conversion matrix on the performance. To test this the sensor is rotated about an angle of about 45° around the z axis. The exact value can be determined from the conversion matrix

$$a = \begin{pmatrix} 5.4090 & 6.3039 & 0.0188 \\ -5.4984 & 5.5221 & -0.0097 \\ 0.0744 & 0.1257 & 8.0394 \end{pmatrix} \Leftrightarrow a^{-1} = \begin{pmatrix} 0.0856 & -0.0977 & -0.0003 \\ 0.0852 & 0.0838 & -0.0001 \\ -0.0021 & -0.0004 & 0.1244 \end{pmatrix}. \tag{4.5}$$

If the angle would be perfectly 90 degrees to the ideal angle the PID should not work at all without the coupling of the single PIDs. In this case the x PID would only measure the impact of the value that the y PID has caused and therefore can not verify, measure and control the magnetic field in its direction. If the PID is aligned perfectly then the impact of each controller is only read by each controller which would make it perform ideal. Any value in between leads to a mixed pick up of the x and y controller by each PID in these directions. This leads the fact that the stabilisation is still possible, but not ideal. One controller would try to compensate the compensation of the other one and so on. This fact can be seen in Fig. 39. The controller with the compensation matrix, should perform like an controller without this matrix in a perfect aligned position. Recorded curve crosses the magnetic background noise at around 150 Hz. This is indeed the same value that was observed with a good aligned sensor, Fig. 36, where the conversion matrix has in good approximation only values on the diagonal. In this case the matrix has low impact and can be seen as negligible. The increase of the amplitude at higher frequencies is also similar to the one in perfect alignment. The alignment was in this case far away from perfect and at an angle of $\approx 45°$. The intersection of the PID with no conversion matrix lies at around 75 Hz, which is half of the value that the ideal case produces.

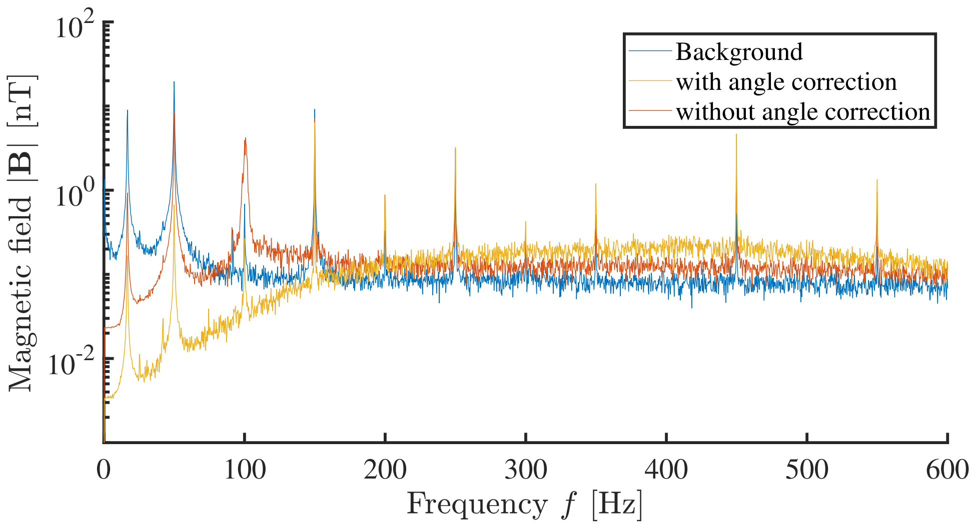

Figure 39: Fast Fourier transformation of the magnetic field fluctuations inside the coil cage with a sensor rotated 45° around the z axis. One measurement was taken with angle correction matrix and the second one without.

The result of this comparison shows that the use of a conversion matrix can make the PID system operate on the same level as it would with perfect alignment. The orientation can be chosen randomly, without any performance issues, as long as the conversion matrix is recorded at this position. A PID system without this matrix could also work, if the sensor and the coils are well aligned, but it will have performance losses. This result is specifically interesting for three traditional analog PIDs.

5 Summary and Outlook

The results presented in this thesis built the foundation to compare an active magnetic field stabilization for a quantum gas microscope against a passive shielded option.
The chosen design consist of three completely equal square Helmholtz coils. Each of them has a side length a of 36,7 cm and the a spacing d to the corresponding one of 20.0 cm, to create the largest possible area of a homogeneous magnetic field. The number of turns n was chosen to be 3, so that the possible produced magnetic field is around ten times the amplitude of the field fluctuations. All three coils produce a magnetic field per current of

$$B/I = 107(4)\,\mu\mathrm{T}/A = 1070(40)\,\mathrm{mG}/A. \tag{5.1}$$

This result fits the expected theory value. The measured impedance of a single coil pair, with an additional $1\,\Omega$ resistor to enable sufficient voltage control was

$$L = 13.4(5)\,\mu\mathrm{H}. \tag{5.2}$$

This contributes to a 3 dB point of one total square Helmholtz pair of 6.5 Hz. All properties qualify the coils for the intended stabilisation.
The used sensor was the FLC3-70 sensor from Stefan Mayer Instruments with a precision up to $0.5\,\mathrm{nT_{rms}}$. It allows a magnetic field measurements in all three directions valid to frequencies of 1 kHz. The reading of the whole digital PID system, made of a ADC, DAC and a microcontroller, had a noise that translates to $3\,\mathrm{nT_{rms}}$. With this it was able to compensate a magnetic background noise from 39 nT to a stable field of

$$\Delta B_{\mathrm{rms}} = 8\,\mathrm{nT} \tag{5.3}$$

deviation in one direction. The maximum effective frequency was 200 Hz.
To stabilise the magnetic field in all three directions a conversion matrix was digitally inserted in the PID code to compensate the coupling of the one measurement axis to all three coils that produce the magnetic field. The stabilisation in all three directions lead to a reduction of the total magnetic background field noise of 26 nT to a value of

$$\Delta|\mathbf{B}|_{\mathrm{rms}} = 11\,\mathrm{nT} \tag{5.4}$$

with active stabilisation. The maximum effective frequency decreases to 150 Hz, which is also caused by the reduced absolute frequency per single channel.
These values characterise the coil system and the PID. This thesis also shows multiple routes for further improvements that could be done in continued investigations. The most obvious change is to swap the voltage controlled power supply to an intended current controlled PSU. Also the measured time delay of $178(4)\,\mu$s is the second approach for improvements. It can be reduced, if the main contributor, the ADC AD4111 is eliminated. A possible option is to swap this component to a similar, but faster one. Another option to decease the response time and also increase the sampling frequency is to change to an analog PID system. This one has to have a analog conversion matrix to compensate the orientation of the sensor. A hybrid system where the PID constants and set points are determined by a digital controller but the computing of the PID loop is done by an analog PID, would combine the huge flexibility of the digital solution with a possibly faster analog PID loop. Another different solution can be offered. A field programmable gate array (FPGA) could be used to perform the ADC, DAC and PID all at once.

6 References

[1]J. Hertkorn, J. Schimdt, F. Böttcher, M. Gou, M. Schmidt, K. Ng, S. Graham, H. Büchler, T. Langen, M. Zwierlein, and T. Pfau, “Density Fluctuations across the Superfluid-Supersolid Phase Transition in a Dipolar Quantum Gas”, Phys. Rev. X **11**, 011037 (2021).

[2]J. Schimdt, J. Hertkorn, M. Gou, F. Böttcher, M. Schmidt, K. Ng, S. Graham, T. Langen, M. Zwierlein, and T. Pfau, “Roton Excitations in an Oblate Dipolar Quantum Gas”, Phys. Rev. Lett. **126**, 193002 (2021).

[3]W. Martin, Z. Romuland, and L. Hagan, *Atomic Energy Levels–The Rare-Earth Elements* (U.S. Department of Commerce, 1978).

[4]M. Lu, N. Q. Burdick, S. H. Youn, and B. L. Lev, “A Strongly Dipolar Bose-Einstein Condensate of Dysprosium”, Phys. Rev. Lett. **107**, 190401 (2011).

[5]J. Hertkorn, J. Schimdt, M. Gou, F. Böttcher, K. Ng, S. Graham, P. Uerlings, T. Langen, M. Zwierlein, and T. Pfau, “Pattern Formation in Quantum Ferrofluids: from Supersolids to Superglasses”, Phys. Rev. Res. **3**, 033125 (2021).

[6]R. P. Feynman, “Simulating Physics with Computers”, Int. J. Theor **21**, 467–488 (1982).

[7]J. D. Jackson, *Klassische Elektrodynamik* (De Gruyter, Berlin, 2014).

[8]P. A. Tipler, G. Mosca, and J. Wagner, *Physik für Wissenschaftler und Ingenieure* (Springer Spektrum, 2015).

[9]M. C. Wapler, J. Leupold, I. Dragonu, D. von Elverfeld, M. Zaitsev, and U. Wallrabe, “Magnetic properties of materials for MR engineering, micro-MR and beyond”, Journal of Magnetic Resonance **242C**, 233–242 (2014).

[10]A. Restrepo, E. Franco, H. Cadavid, and C. Pinedo, “A comparative study of the magnetic field homogeneity for circular, square and equilateral triangular Helmholtz coils”, Conference Paper (2017).

[11]A. H. Firester, “Design of Square Helmholtz Coil Systems”, Rev. Sci. Instrum. **37**, 1264–1265 (1699).

[12]R. Hurtado-Velasco and J. Gonzalez-Llorente, “Simulation of the magnetic field generated by square shape Helmholtz coils”, Applied Mathematical Modelling **40**, 9835–9847 (2016).

[13]M. Misakian, “Equations for the Magnetic Field Produced by One or More Rectangular Loops of Wire in the Same Plane”, J. Res. Natl. Inst. Stand. Technol. **105**, 557 (2000).

[14]J. J. Abbott, “Parametric design of tri-axial nested Helmholtz coils”, Rev. Sci. Instrum. **86**, 054701 (2015).

[15]*OPA548 High-Voltage, High-Current Operational Amplifier*, English, OPA548, version Rev. D, Texas Instruments (2019).

[16]M. Wenzel, “Aktive Magnetfeldkompensation für atomoptische Experimente”, Bachelor’s Thesis (2012).

[17] *Laboratory Power Supply EA-PS 3016-20 B*, German, EA-PS 3016-20 B, version Rev. 0, Elektro-Automatik (2021).

[18] M. A. Johnson and M. H. Moradi, *PID Control, New Identification and Design Methods* (Springer-Verlag, 2005).

[19] G. J. Silva, A. Datta, and S. Bhattacharyya, *PID Controls for Time-Delay Systems* (Birkenhäuser, 2005).

[20] M. Chidambaram and N. Saxena, *Relay Tuning of PID Controllers* (Springer-Verlag, 2005).

[21] F. M. Förester, *Method and apparatus for non destructive testing*, U.S. Patent 2 901 691 (1659).

[22] *Magnetfeldsensor FLC3-70*, German, FLC3-70, version Rev. 0, Stefan Mayer Instruments (2021).

[23] *Single Supply, 24-Bit, Sigma-Delta ADC with ±10 V and 0 mA to 20 mA Inputs, Open Wire Detection*, English, AD4111, version Rev. B, Analog Devices (2021).

[24] *DACx1408 8-Channel, 16-,14-,12-Bit, High-Voltage Output DACs with Internal Reference*, English, DACx1408, version Rev. A, Texas Instruments (2018).

[25] J. Ziegler and N. Nichols, "Optimum Settings for Automatic Controllers", Transactions of the A.S.M.E., 749–765 (1942).